Crack-induced electrical resistivity changes in cracked CNT-reinforced composites

L. Rodríguez-Tembleque*[1], F. García-Sánchez[2], E. García-Macías[3], F.C. Buroni[1], A. Sáez[1]

[1] *Escuela Técnica Superior de Ingeniería, Universidad de Sevilla, Camino de los Descubrimientos s/n , Sevilla 41092, Spain.*

[2] *Escuela de Ingenierías Industriales, Universidad de Málaga, Doctor Ortiz Ramos s/n, Málaga 29071, Spain.*

[3] *Department of Civil and Environmental Engineering, University of Perugia, Via G Duranti 93, Perugia 06125, Italy.*

Abstract

Carbon nanotube (CNT)-reinforced composites exhibit a piezoresistive behavior that permits their use as sensors in novel structural health monitoring (SHM) applications, by measuring the electrical resistivity change of the CNT modified laminate. However, the presence of cracks in such composite materials may not only compromise their structural integrity, but may as well alter their capability to act as reliable piezoresistive sensors. In this paper, we conduct a numerical study aimed at quantifying how the presence of cracks in reinforced polymer composites does influence their electrical conductivity and, consequently, their sensor performance. To this end, the electromechanical constitutive properties of the composite are determined by a mixed micromechanics approach that allows characterizing both the elastic properties and the strain-induced alterations in the overall electrical conductivity of the CNT-reinforced composite. The strain response of the cracked composite domain is accurately determined by means of a dual Boundary Element (BE) approach. Electrical conductivity in the cracked composite follows from its computed strain state at each point in the domain. Subsequently, the resulting non-homogeneous electrical conductivity problem is solved using a finite differences scheme that also accounts for semipermeable crack-face electrical boundary conditions. Several parametric studies are conducted to illustrate the influence of various crack geometries in the piezoresistive behavior of CNT-reinforced composites at varying CNTs concentrations.

Key words: Carbon Nanotube, Crack detection, Nanocomposites, Piezoresistivity, Damage identification.

1. Introduction

Over the past fifteen years, composite materials fabricated by dispersing various carbon nano-scale fillers into a polymeric matrix, say for example graphene nanoplatelets or CNTs, have attracted enormous attention from the scientific community. This is due to the fact that the electrical conductivity properties that such fillers confer to the otherwise non-conductive matrix, make them good candidates as sensors for novel SHM applications. CNTs do not only reinforce the base matrix material by greatly improving its overall mechanical properties, but also have the capability of forming minimally invasive- electrically conductive networks that enable strain sensing [1, 2, 3, 4, 5, 6], all of it by adding quite low CNT filler contents. Recent advances on fabrication and testing of CNT-reinforced composites ensure repeatability and stability of this new class of piezo-resistive sensors and establish them as an actual alternative for SHM [7, 8, 9, 10, 11, 12, 13]. For instance, previous works by the authors have satisfactorily illustrated the expected performance of multi-walled CNTs (MWCNT)/epoxy strip-like strain sensors for buckling detection in beam structures [14] and for crack detection and localization in reinforced concrete beams [15].

In this context, it is crucial to develop tools for assessing the structural integrity of the sensor itself, as cracks may appear within the MWCNT/epoxy strip sensor during its service life. In such a case, the problem that we face is

*corresponding author

Email address: luisroteso@us.es (L. Rodríguez-Tembleque[1])

twofold: the presence of a crack in the sensor will not only compromise its integrity, but it may significantly modify its sensing capability and therefore could lead to the adoption of wrong maintenance measures in a SHM framework. All of it, bearing in mind that addition of CNTs to the epoxy matrix does also contribute to improve the composite fracture toughness and the energy release by bridging up the crack faces, as previous experimental [16, 17, 18, 19, 20, 21, 22] and numerical works reveal [23, 24, 25, 26]. However, most of these works focus on analyzing the improvement of the fracture behavior of the CNT-reinforced polymer composite from a mechanical perspective.

In this paper, we conduct a numerical study that aims at characterizing the change in electrical conductivity induced in a MWCNTs/epoxy composite by the presence of several crack configurations at varying CNTs volume fractions, with the objective of assessing how the performance of the CNT-epoxy sensor is affected by cracking. To this end, the dual BE formulation previously developed by García-Sánchez et al. [27] for fracture mechanics applications is employed herein, provided the ability of the BE method to model high stress gradients accurately and efficiently in the context of linear elastic fracture mechanics problems [28, 29].

The implemented dual BE formulation is based on both the displacement and traction boundary integral equations, together with an efficient regularization procedure that permits to deal with the singular and hypersingular integrals in a straightforward manner. Discontinuous quarter-point elements are used to accurately evaluate the relevant fracture parameters. The constitutive electro-mechanical modeling of the MWCNTs/epoxy composite follows a two-step procedure, whose details may be consulted elsewhere [14, 15]. In essence, provided that piezo-resistivity is a one-way coupled electro-mechanical property, we first conduct the homogenization of the mechanical properties by applying a mean-field approach that takes into account the interfacial effects that characterize the load transfer mechanisms at the epoxy matrix/MWCNT interfaces. The second step tackles the homogenization of the electrical conductivity and piezo-resistivity properties, implementing the model proposed by García-Macías et al. [30] and further adjusting the parameters of such micromechanics model to fit experimental results available in the literature [14, 15]. In this way, the dual BE approach computes the strain state in the cracked domain and, subsequently, strains can be directly related to local changes in piezo-resistivity. The resulting non-homogeneous electrical conductivity problem is then solved using a finite differences scheme, in order to correlate the crack damage observed in a MWCNT/epoxy strip-like strain sensor with the electrical resistance change measured between electrodes. The proposed numerical framework permits to solve the problem for different crack-face electric permittivity boundary conditions, ranging from impermeable crack conditions to fully permeable crack conditions. Several parametric studies are presented and discussed in detail that reveal how the presence of cracks does significantly alter the piezo-resistive behavior of the MWCNTs/epoxy composite strain sensors.

2. Micromechanics modeling of MWCNT/epoxy nanocomposites

This section concisely overviews the micromechanics modeling of the electromechanical constitutive properties of strain self-sensing MWCNT/epoxy nanocomposites. For notational convenience, blackboard bold letters are used to denote fourth-order tensors $\mathbb{A} = A_{ijkl}$, while bold letters indicate second-order tensors $\mathbf{A} = A_{ij}$. A colon between two fourth-order tensors denotes inner product, $(\mathbb{A} : \mathbb{B})_{ijmn} \equiv A_{ijkl}B_{klmn}$.

2.1. Mechanical properties of MWCNT/epoxy nanocomposites

Let us assume a Representative Volume Element (RVE) of an epoxy matrix doped with a sufficient number of MWCNTs to statistically represent the composite as a whole. The geometrical dimensions of MWCNTs, that is length L_{cnt} and diameter D_{cnt}, are assumed constant throughout the RVE. The orientation of the fillers is unequivocally defined by two Euler angles, θ and γ as shown in Fig. 1 (a). In order to take into account the filler/matrix interfacial properties, a core-shell interphase model [31, 32] is adopted. This approach assumes that interfacial properties can be idealized as finite elastic coatings with constant thickness t surrounding the fillers. Therefore, the composite is defined as a three-phase composite including the matrix, inclusions and interphases with elastic tensors $\mathbb{C}_m$, $\mathbb{C}_p$ and $\mathbb{C}_i$. Indexes "p", "i", and "m" relate the corresponding quantity to the filler, interphase and matrix phases, respectively. According to the double inclusion methodology by Hori and Nemat-Nasser [33], the effective stiffness tensor of the composite reads:

$$\overline{\mathbb{C}} = \left(f_m\mathbb{C}_m + f_i\left\langle\mathbb{C}_i : \mathbb{A}_i\right\rangle + f_p\left\langle\mathbb{C}_p : \mathbb{A}_p\right\rangle\right) : \left(f_m\mathbb{I} + f_i\left\langle\mathbb{A}_i\right\rangle + f_p\left\langle\mathbb{A}_p\right\rangle\right)^{-1}, \tag{1}$$

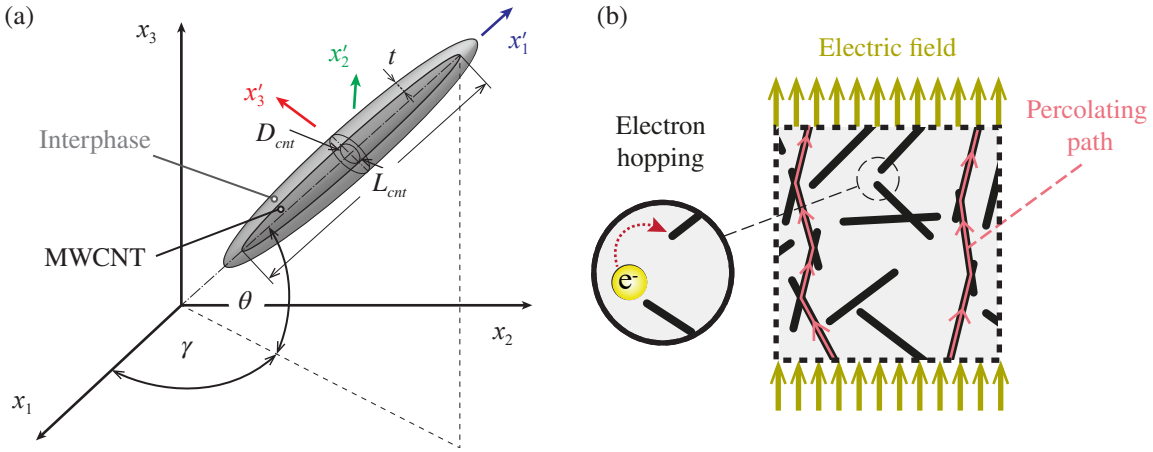

Figure 1: (a) Euler angles defining the relation between the orientation of a MWCNT in the local coordinate system, K′ ≡ $\{0; x_1' x_2' x_3'\}$ and the global coordinate system, K≡ $\{0; x_1 x_2 x_3\}$. (b) Schematic representation of the contribution of electron hopping and conductive networking mechanisms to the overall electrical conductivity of MWCNT/epoxy nanocomposites.

with f_p, f_i, and f_m being the volume fractions occupied by the fillers, the interphases and the host matrix, respectively. MWCNT/epoxy interfaces are characterized by weak van der Waals (vdW) forces, thereby penetrable soft interphases are assumed in this work, and the expression of their volume fraction f_i reads [14, 34]:

$$f_i = (1-f_p)\left(1-\exp\left\{-\frac{6f_p}{1-f_p}\left[\frac{\eta}{n(\kappa)}+\left(2+\frac{3f_p}{n^2(\kappa)(1-f_p)}\right)\eta^2+\right.\right.\right.$$
$$\left.\left.\left.+\ \frac{4}{3}\left(1+\frac{3f_p}{n(\kappa)(1-f_p)}\right)\eta^3\right]\right\}\right), \tag{2}$$

where term η denotes the ratio of the thickness of the interphases t and the equivalent diameter D_{eq} (i.e. $\eta = t/D_{eq}$). The equivalent diameter defines the diameter of an equivalent sphere having the same volume as that of the particles. Assuming that MWCNTs have an aspect ratio $s = L_{cnt}/D_{cnt} > 1$, D_{eq} takes the form $D_{eq} = D_{cnt}s^{1/3}$ [14, 34]. The term $n(s)$ stands for the sphericity of the fillers and is defined as:

$$n(s) = \frac{2s^{2/3}\tan\varphi}{\tan\varphi + s^2\varphi}, \tag{3}$$

where φ is given by $\varphi = \arccos(1/s)$. Terms $\mathbb{A}_i$ and $\mathbb{A}_p$ in Eq. (1) denote the concentration tensors for interphases and inclusions, respectively, and can be expressed in terms of the corresponding dilute concentration tensors, $\mathbb{A}_i^{dil}$ and $\mathbb{A}_p^{dil}$, as:

$$\mathbb{A}_\chi = \mathbb{A}_\chi^{dil} : \left(f_m\mathbb{I} + f_i\mathbb{A}_i^{dil} + f_p\mathbb{A}_p^{dil}\right)^{-1}, \quad \chi = p, i \tag{4}$$

$$\mathbb{A}_\chi^{dil} = \mathbb{I} + \mathbb{S} : \mathbb{T}_\chi, \quad \chi = p, i \tag{5}$$

with

$$\mathbb{T}_\chi = -\left(\mathbb{S} + \mathbb{M}_\chi\right)^{-1}, \quad \chi = p, i \tag{6}$$

$$\mathbb{M}_\chi = \left(\mathbb{C}_\chi - \mathbb{C}_m\right)^{-1} : \mathbb{C}_m, \quad \chi = p, i \tag{7}$$

where $\mathbb{S}$ denotes the mechanical fourth-order Eshelby's tensor, whose formulation for prolate ellipsoidal particles can be found elsewhere [35]. Angle brackets $\langle\cdot\rangle$ in Eq. (1) indicate orientational average weighted by an orientation distribution function (ODF) $\Omega(\gamma,\theta)$. Unless special aligning techniques are undertaken, fillers are usually randomly oriented throughout the composite, and the ODF is constant within the whole Euler space.

2.2. Electrical conductivity of MWCNT/epoxy nanocomposites

Most literature works agree to define the electrical behavior of MWCNT-based composites as percolation-type, according to which their electrical conductivity experiences a rapid increase of several orders of magnitude when the filler concentration reaches a certain percolation threshold, f_c. Below percolation ($f_p < f_c$), fillers are very distant and electrons can only be transferred through a quantum tunneling effect, also known as electron hopping mechanism. Once the filler volume fraction reaches the percolation threshold ($f_p \geq f_c$), some fillers begin forming electrically conductive paths and the overall conductivity is governed by both electron hopping and conductive networking mechanisms as sketched in Fig. 1 (b). The fraction of percolated MWCNTs, ξ_p, can be approximated as [36]:

$$\xi_p = \begin{cases} 0, & 0 \leq f_p < f_c \\ \dfrac{f_p^{1/3} - f_c^{1/3}}{1 - f_c^{1/3}}, & f_c \leq f_p \leq 1 \end{cases} \tag{8}$$

The electron hopping mechanism can be taken into account by conductive interphases, whilst the conductive networking mechanism can be simulated through variations of the filler aspect ratio [37]. The electrical resistivity of the interphases is commonly computed by the generalized Simmons' formula [38]:

$$R_{int}(d_a) = \frac{d_a \hbar^2}{a e^2 \left(2m\lambda^{1/2}\right)} \exp\left(\frac{4\pi d_a}{\hbar}\left(2m\lambda\right)^{1/2}\right), \tag{9}$$

where m and e are the mass and the electric charge of the electron, respectively, λ is the height of the tunneling potential barrier, a is the contact area of the fillers, $\hbar$ stands for the reduced Planck's constant, and d_a is the average inter-particle distance. Being d_c the maximum filler separation for tunneling penetration of electrons, d_a is usually approximated in a piecewise form [37] as d_c and $d_c\left(f_c/f_p\right)^{1/3}$ below and above percolation, respectively. The thickness of the conductive interphases t_c, their electrical conductivity κ_{int}, and the volume fraction f_{eff} of the effective fillers (MWCNTs plus interphases) can be computed as [39, 37]:

$$t_c = \frac{1}{2} d_a, \quad \kappa_{int} = \frac{d_a}{a R_{int}(d_a)}, \quad f_{eff} = \frac{\left(D_{cnt} + 2t_c\right)^2 \left(L_{cnt} + 2t_c\right)}{D_{cnt}^2 L_{cnt}} f_p. \tag{10}$$

On this basis, MWCNT/interphase ensembles can be modeled through equivalent solid cylinders with transversely isotropic conductivity tensor $\boldsymbol{\kappa}_c$(for more detailed information in this regard, readers may refer to [40, 37]). Hence, the overall electrical conductivity of the RVE can be estimated by the Mori-Tanaka method as [41, 42]:

$$\boldsymbol{\kappa}_{eff} = \boldsymbol{\kappa}_m + (1 - \xi_p)\left\langle \boldsymbol{\Gamma}_{EH} \right\rangle + \xi_p \left\langle \boldsymbol{\Gamma}_{CN} \right\rangle, \tag{11}$$

where $\boldsymbol{\kappa}_m$is the conductivity tensor of the matrix phase, and the matrices $\boldsymbol{\Gamma}_{EH}$ and $\boldsymbol{\Gamma}_{CN}$ read:

$$\boldsymbol{\Gamma}_{EH} = f_{eff}\left(\boldsymbol{\kappa}_{EH} - \boldsymbol{\kappa}_m\right)\mathbf{A}_{EH}, \tag{12a}$$

$$\boldsymbol{\Gamma}_{CN} = f_{eff}\left(\boldsymbol{\kappa}_{CN} - \boldsymbol{\kappa}_m\right)\mathbf{A}_{CN}, \tag{12b}$$

with subscripts EH and CN referring to the electron hopping and conductive networking mechanisms, respectively. Nanotubes forming conductive networks can be modeled as fillers with infinite aspect ratio [39]. Therefore, quantities related to the electron hopping mechanism are defined with the actual filler aspect ratio (L_{cnt}/D_{cnt}), while those related to the conductive networking mechanism are defined with infinite filler aspect ratio ($L_{cnt}/D_{cnt} \to \infty$). Finally, the electric field concentration tensor, $\mathbf{A}$, is defined as [37]:

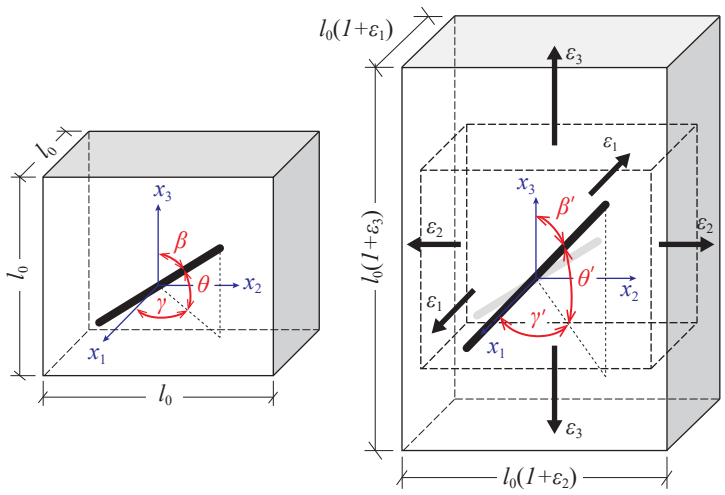

Figure 2: Cubic cell containing an embedded filler and deformed under a tri-axial strain state $(\varepsilon_1, \varepsilon_2, \varepsilon_3)$.

$$\mathbf{A} = \mathbf{A}^{dil} \left\{ \left(1 - f_{eff}\right) \mathbf{I} + f_{eff} \left\langle \mathbf{A}^{dil} \right\rangle \right\}^{-1}, \tag{13}$$

with $\mathbf{I}$ being the second-order identity tensor. Assuming ellipsoid inclusions with symmetric axis x_3, tensors $\mathbf{A}^{dil}$ and $\mathbf{S}$ denoting the dilute electric field concentration and the Eshelby's tensors read [43]:

$$\mathbf{A}^{dil} = \left\{ \mathbf{I} + \mathbf{S} \left(\boldsymbol{\kappa}_m\right)^{-1} \left(\boldsymbol{\kappa}_c - \boldsymbol{\kappa}_m\right) \right\}^{-1}, \tag{14}$$

$$\begin{aligned} S_{22} = S_{33} &= \begin{cases} \dfrac{s}{2\left(s^2-1\right)^{3/2}} \left[s\left(s^2 - 1^{1/2}\right) - \cosh^{-1} s \right]; & s \geq 1 \\ \dfrac{s}{2\left(s^2-1\right)^{3/2}} \left[\cos^{-1} s - s\left(1 - s^2\right)^{1/2} \right]; & s \geq 1 \end{cases} \\ S_{11} &= 1 - 2S_{22}. \end{aligned} \tag{15}$$

2.3. Piezoresistivity properties of MWCNT/epoxy nanocomposites

As pointed out above, the addition of MWCNT into the epoxy matrix does not only reinforce the base matrix material by improving its mechanical properties, but it does also lead to the formation of minimally invasive electrically conductive networks that confer a piezoresistive behavior to the resulting material. The piezoresistive effect refers to the change in the electrical resistivity experienced by a semiconductor when subjected to mechanical strain [44]. In contrast to the piezoelectric effect, the piezoresistive effect causes a change only in the electrical resistance, but not in the electrical potential.

In this manner, it is possible to quantify changes in the strain state of the material by recording changes in its electrical resistance. The strain self-sensing capability of MWCNT/epoxy composites can be simulated by means of strain-induced tampering of the electron hopping and conductive networking mechanisms. Specifically, three major strain effects are usually pointed out in the literature [45, 30], including (i) volume expansion and reorientation of MWCNTs, (ii) breakage of conductive paths, and (iii) variation of the inter-particle properties.

- *Volume expansion and reorientation*:

  Let us consider a deformable l_0-sided cubic cell loaded with a MWCNT as sketched in Fig. 2. When the cell is subjected to an arbitrary dilation strain $(\varepsilon_1, \varepsilon_2, \varepsilon_3)$, its volume changes from $V_0 = l_0^3$ to $V = l_0^3 \overline{\varepsilon}_1 \overline{\varepsilon}_2 \overline{\varepsilon}_3$, with

$\overline{\varepsilon}_i = 1 + \varepsilon_i$. Owing to the considerably stiffer behavior of MWCNTs, the deformation is primarily sustained by the matrix and, as a result, the apparent filler content varies as:

$$f^* = \frac{V_0 f}{V} = \frac{f}{\overline{\varepsilon}_1 \overline{\varepsilon}_2 \overline{\varepsilon}_3}. \tag{16}$$

Additionally, the embedded MWCNT also experiences reorientation as an effect of the applied dilation, which is defined by the change of the Euler angles from (γ, β) to (γ', β') (see Fig. 2). The closed-form expression of the strain-dependent ODF under general dilation strains, $\Omega(\gamma', \beta')$, was recently derived by the authors in [30] as:

$$\Omega(\gamma', \beta') = \frac{\overline{\varepsilon}_1^2 \overline{\varepsilon}_2^2 \overline{\varepsilon}_3^2}{\left[\overline{\varepsilon}_2^2 \overline{\varepsilon}_3^2 \cos^2\beta' + \overline{\varepsilon}_1^2 \left(\overline{\varepsilon}_2^2 \cos^2\gamma' + \overline{\varepsilon}_3^2 \sin^2\gamma'\right) \sin^2\beta'\right]^{3/2}}. \tag{17}$$

The deformable cell model can be also applied to study the effects of distortion. In this case, distortion does not originate volume expansion although it does induce filler reorientation. In the particular case of ε_{32}, the polar angle changes from β to β', while the azimuthal angle remains unchanged. The closed-form expression of the resulting ODF was also derived by the authors as [30]:

$$\Omega(\gamma, \beta') = \left(1 - 4\varepsilon_{32} \sin\gamma \sin\beta' \cos\beta' + 4\varepsilon_{32}^2 \sin\gamma \sin\beta'\right)^{-3/2}. \tag{18}$$

- *Breakage of conductive paths*:

  The strain-induced filler reorientation reduces the randomness of the MWCNTs' dispersion and, as a consequence, the likelihood of forming conductive networks decreases, that is to say, the percolation threshold increases. Such a variation can be included in terms of the previously outlined strain-dependent ODFs as shown by the authors in reference [30] through the stochastic percolation model of Komori and Makishima [46].

- *Variation of the inter-particle properties*:

  Mechanical strains also have a direct effect on the electron hopping mechanism. In particular, assuming that deformations are mainly sustained by the matrix phase, mechanical strains primarily affect the inter-particle distance and the height of the potential barrier. At low strain levels ($< 10^{-4}$), some research studies in the literature consider that the inter-particle distance, d_a, and the height of the potential barrier, λ, vary linearly with strain as [47]:

$$\begin{aligned} d_a &= d_{a,0}(1 + C_1\varepsilon), \\ \lambda &= \lambda_0(1 + C_2\varepsilon), \end{aligned} \tag{19}$$

  where subscript 0 relates the corresponding quantities to the unstrained system, and C_1 and C_2 are proportionality constants. Given the difficulty involved in their determination, C_1 and C_2 are usually computed by fitting experimental data.

Finally, the modeling of the piezoresistivity of MWCNT-based composites can be readily conducted by combining the previously outlined micromechanics approach in Section 2.2 and the indicated strain-induced effects. For notational simplicity, the overall electrical resistivity tensor, $\boldsymbol{\rho}_{eff} = \boldsymbol{\kappa}_{eff}^{-1}$, is written in matrix notation as:

$$\boldsymbol{\rho}_{eff} = \begin{bmatrix} \rho_1 & \rho_6 & \rho_5 \\ \rho_6 & \rho_2 & \rho_4 \\ \rho_5 & \rho_4 & \rho_3 \end{bmatrix}. \tag{20}$$

In the absence of mechanical strains, MWCNTs are randomly oriented, and $\boldsymbol{\rho}_{eff}$ takes the form of a diagonal matrix with components $\rho_1 = \rho_2 = \rho_3 = \rho_0$ and $\rho_4 = \rho_5 = \rho_6 = 0$. Once the composite is subjected to a mechanical strain, the relative change in resistivity can be related to the mechanical strain tensor $\boldsymbol{\varepsilon}$ as [30]:

$$\begin{bmatrix}\Delta\rho_1/\rho_0\\ \Delta\rho_2/\rho_0\\ \Delta\rho_3/\rho_0\\ \Delta\rho_4/\rho_0\\ \Delta\rho_5/\rho_0\\ \Delta\rho_6/\rho_0\end{bmatrix} = \begin{bmatrix}\lambda_{11} & \lambda_{12} & \lambda_{12} & 0 & 0 & 0\\ \lambda_{12} & \lambda_{11} & \lambda_{12} & 0 & 0 & 0\\ \lambda_{12} & \lambda_{12} & \lambda_{11} & 0 & 0 & 0\\ 0 & 0 & 0 & \lambda_{44} & 0 & 0\\ 0 & 0 & 0 & 0 & \lambda_{44} & 0\\ 0 & 0 & 0 & 0 & 0 & \lambda_{44}\end{bmatrix}\begin{bmatrix}\varepsilon_1\\ \varepsilon_2\\ \varepsilon_3\\ 2\varepsilon_{23}\\ 2\varepsilon_{13}\\ 2\varepsilon_{12}\end{bmatrix}, \tag{21}$$

where the terms λ_{ij} denote the piezoresistivity coefficients. Specifically, λ_{11} represents the longitudinal piezoresistive effect, λ_{12} relates the transverse piezoresistive effect, and λ_{44} describes the effect on an out-of-plane electric field by the change of the in-plane current induced by in-plane shear stress. All the piezoresistivity coefficients λ_{ij} can be obtained by two virtual experiments using the previously outlined micromechanics approach, including a laterally constrained uni-axial dilation test and a distortion test (interested readers may refer to [30] for further theoretical details).

3. Basic formulae and numerical implementation

3.1. Governing equations

This work considers a two-dimensional, homogeneous, elastic and linear fractured FRP domain $\Omega \subset \mathbb{R}^2$ with boundary $\partial\Omega$, in a Cartesian coordinate system (x_i) $(i = 1, 2)$. The boundary $\partial\Omega$ is divided in two disjoint parts: $\partial\Omega = \partial\Omega_e \cup \partial\Omega_c$, where $\partial\Omega_e$ denotes the external boundary and $\partial\Omega_c$ is the crack surface. The boundary $\partial\Omega_e$ is eventually divided in two partitions: $\partial\Omega_e = \partial\Omega_u \cup \partial\Omega_p$, with $\partial\Omega_u$ being the external boundary on which displacements $\tilde{u}_i$ are prescribed and $\partial\Omega_p$ its counterpart with imposed tractions $\tilde{p}_i$. Moreover, the crack surface is constituted by the upper and lower crack faces, i.e., $\partial\Omega_c = \partial\Omega_c^+ \cup \partial\Omega_c^-$ (see Fig.3), where the crack surface tractions (i.e., p_i^+ and p_i^-) depend on the crack opening conditions (the superscripts + and − stand for the upper and lower crack surfaces).

Assuming static loading conditions, the mechanical equilibrium equations on Ω, in the absence of body forces, are

$$\begin{array}{lll}\sigma_{ij,j} = 0 & \text{in} & \Omega,\\ \sigma_{ij}n_j = \tilde{p}_i & \text{on} & \partial\Omega_p,\\ \sigma_{ij}n^+_{c,j} = p_i^+ & \text{on} & \partial\Omega_c^+,\\ \sigma_{ij}n^-_{c,j} = p_i^- & \text{on} & \partial\Omega_c^-,\end{array} \tag{22}$$

with σ_{ij} being the components of Cauchy stress tensor, n_i the unit normal on $\partial\Omega_p$, $n^+_{c,i}$ being the unit normal on the upper crack face $\partial\Omega_c^+$ and $n^-_{c,i}$ the unit normal on the lower face $\partial\Omega_c^-$. Finally, the stress and strain tensors for a general linear elastic material are coupled through the following constitutive law

$$\sigma_{ij} = C_{ijkl}\varepsilon_{kl}, \tag{23}$$

where the infinitesimal strain tensor ε_{ij} can be obtained from derivatives of the displacements field u_i in Ω as: $\varepsilon_{kl} = (u_{k,l} + u_{l,k})/2$ and C_{ijkl} denotes the components of the elastic stiffness tensor, which satisfies the following symmetries: $C_{ijkl} = C_{jikl} = C_{ijlk} = C_{klij}$ and it is positive definite.

3.2. Boundary element formulation

Let us consider a two-dimensional, homogeneous and linear fiber-reinforced fractured composite $\Omega \subset \mathbb{R}^2$ with boundary $\partial\Omega = \partial\Omega_e \cup \partial\Omega_c$. To overcome the difficulty of having two coincident boundaries on the crack surfaces $\partial\Omega_c = \partial\Omega_c^+ \cup \partial\Omega_c^-$, the dual formulation for the BE solution of crack problems [48, 49] is considered herein. In this manner, a combination of the displacement (DBIE) and the traction (TBIE) boundary integral equations is used to solve crack problems.

The DBIE is applied for collocation points $\boldsymbol{\xi}$ on the crack-free boundary $\partial\Omega_e$ and on either of the crack faces, say $\partial\Omega_c^-$ ($\boldsymbol{\xi} \in \{\partial\Omega_e \cup \partial\Omega_c^-\}$), to yield

$$c_{ij}(\boldsymbol{\xi})u_j(\boldsymbol{\xi}) + \fint_{\partial\Omega} p^*_{ij}(\mathbf{x}, \boldsymbol{\xi})u_j(\mathbf{x})dS(\mathbf{x}) = \int_{\partial\Omega} u^*_{ij}(\mathbf{x}, \boldsymbol{\xi})p_j(\mathbf{x})dS(\mathbf{x}), \tag{24}$$

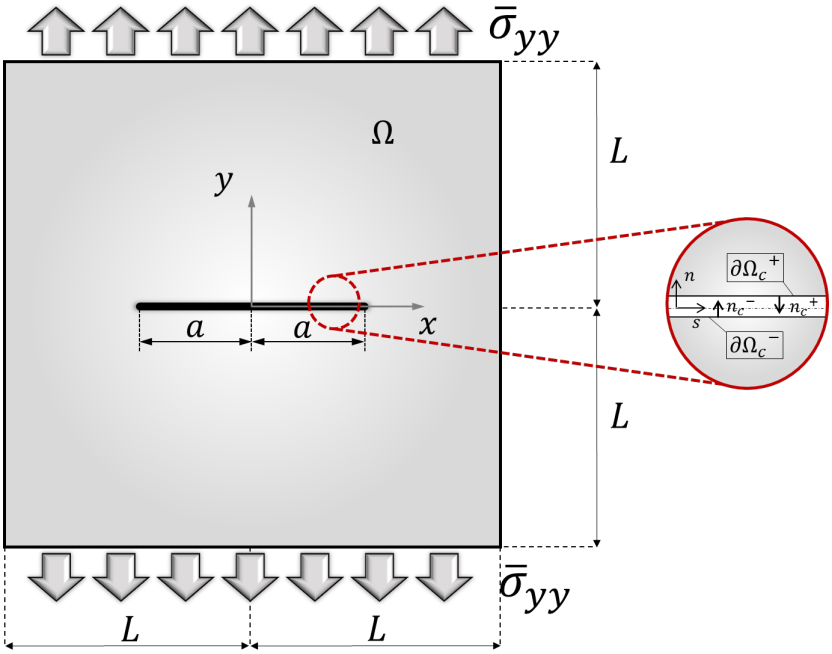

Figure 3: Cracked plate under uniform stress ($\bar{\sigma}_{yy}$).

where $\mathbf{x}$ is a boundary point ($\mathbf{x} \in \partial\Omega$), the symbol $\oint$ stands for the Cauchy Principal Value (CPV) of the integral, u_j is the displacement vector and p_j denotes the crack surface tractions. The free term c_{ij} depends on the local geometry of the boundary $\partial\Omega$ at the collocation point $\boldsymbol{\xi}$; u^*_{ij} and p^*_{ij} are the displacement fundamental solution [27, 49] and the traction fundamental solution at a boundary point $\mathbf{x}$ due to a unit extended source applied at point $\boldsymbol{\xi}$, respectively:

$$u^*_{ij}(z^x_m, z^\xi_m) = -\frac{1}{\pi} Re\left\{\sum_{r=1}^{2} A_{jr}\left[H_{ri}\ln(z^x_r - z^\xi_r)\right]\right\} \tag{25}$$

$$p^*_{ij}(z^x_m, z^\xi_m) = \frac{1}{\pi} Re\left\{\sum_{r=1}^{2} L_{jr}\left[H_{ri}\,\frac{\mu_r n_1 - n_2}{(z^x_r - z^\xi_r)}\right]\right\} \tag{26}$$

In equations (25) and (26), $Re\{\,\}$ stands for the real part, $\mathbf{n} = (n_1, n_2)$ is the outward unit normal at the observation point $\mathbf{x}$ and both the source point, $\mathbf{z}^\xi$, and the observation point, $\mathbf{z}^x$, have been redefined on the complex plane as

$$z^\xi_m = \xi_1 + \mu_m \xi_2 \quad ; \quad z^x_m = x_1 + \mu_m x_2 \quad ; \quad m = 1, 2 \tag{27}$$

with μ_m being the roots of the following characteristic equation:

$$\left|C_{1ij1} + (C_{1ij2} + C_{2ij1})\,\mu_m + C_{2ij2}\,\mu_m^2\right| = 0 \tag{28}$$

where C_{ijkl} are the elastic moduli of the material. For each characteristic root, μ_m, the columns of the matrix $\mathbf{A}$ are obtained from

$$[C_{1ij1} + (C_{1ij2} + C_{2ij1})\,\mu_m + C_{2ij2}\,\mu_m^2]\,A_{jm} = 0 \quad \text{(no sum on } m\text{)} \tag{29}$$

and the components of the $\mathbf{L}$ matrix are given by

$$L_{im} = \sum_{j=1}^{2} [C_{2ij1} + C_{2ij2}\,\mu_m]\,A_{jm} \tag{30}$$

and the terms of matrix $\mathbf{H}$ follow from

$$\mathbf{H} = \mathbf{A}^{-1}(\mathbf{B}^{-1} + \overline{\mathbf{B}}^{-1})^{-1} \quad \text{with} \quad \mathbf{B} = i\mathbf{A}\mathbf{L}^{-1}. \tag{31}$$

The TBIE is applied for collocation points $\boldsymbol{\xi}$ on the other crack surface $\partial\Omega_c^+$ (i.e., $\boldsymbol{\xi} \in \partial\Omega_c^+$) to yield

$$c_{ij}(\boldsymbol{\xi})p_j(\boldsymbol{\xi}) + \oint\!\!\!\!\!\!-_{\partial\Omega} s_{ij}^*(\mathbf{x},\boldsymbol{\xi})u_j(\mathbf{x})dS(\mathbf{x}) = \int_{\partial\Omega} d_{ij}^*(\mathbf{x},\boldsymbol{\xi})p_j(\mathbf{x})dS(\mathbf{x}), \tag{32}$$

to complete the set of equations. Symbols $\oint\!\!\!\!\!\!-$ in Eq.(32) stands for the Hadamard Finite Part (HFP) of the integral and s_{ij}^* and d_{ij}^* are obtained by differentiation of u_{ij}^* and p_{ij}^*, as

$$d_{ij}^*(\mathbf{x},\boldsymbol{\xi}) = -N_s(\boldsymbol{\xi})C_{sikr}u_{kj,r}^*(\mathbf{x},\boldsymbol{\xi}), \tag{33}$$

$$s_{ij}^*(\mathbf{x},\boldsymbol{\xi}) = -N_s(\boldsymbol{\xi})C_{sikr}p_{kj,r}^*(\mathbf{x},\boldsymbol{\xi}), \tag{34}$$

with $N_s(\boldsymbol{\xi})$ being the outward unit normal to the boundary at the source point. The derivatives of the u_{ij}^* and p_{ij}^* at the collocation point are evaluated from

$$u_{ij,k}^*(z_m^x, z_m^\xi) = \frac{1}{\pi}Re\left\{\sum_{r=1}^{2} A_{jr}\left[H_{ri}\ \frac{(\delta_{k1} + \mu_r\,\delta_{k2})}{(z_r^x - z_r^\xi)}\right]\right\}, \tag{35}$$

$$p_{ij,k}^*(z_m^x, z_m^\xi) = \frac{1}{\pi}Re\left\{\sum_{r=1}^{2} L_{jr}\left[H_{ri}\ (\delta_{k1} + \mu_r\,\delta_{k2})\frac{\mu_r n_1 - n_2}{(z_r^x - z_r^\xi)^2}\right]\right\}, \tag{36}$$

where δ_{ij} stands for the Kronecker delta.

Alternatively, when the cracks are mechanically self-equilibrated, i.e., $\Delta p_i = p_i^+ + p_i^- = 0$ on $\partial\Omega_c$, instead of the collocation approach described in equations (24) and (32), it would suffice to apply the DBIE (24) for collocation points $\boldsymbol{\xi}$ on $\partial\Omega_e$ (i.e., $\boldsymbol{\xi} \in \partial\Omega_e$):

$$c_{ij}(\boldsymbol{\xi})u_j(\boldsymbol{\xi}) + \int_{\partial\Omega_e} p_{ij}^*(\mathbf{x},\boldsymbol{\xi})u_j(\mathbf{x})dS(\mathbf{x}) + \int_{\partial\Omega_c^+} p_{ij}^*(\mathbf{x},\boldsymbol{\xi})\Delta u_j(\mathbf{x})dS(\mathbf{x}) = \int_{\partial\Omega_e} u_{ij}^*(\mathbf{x},\boldsymbol{\xi})p_j(\mathbf{x})dS(\mathbf{x}), \tag{37}$$

and the TBIE (32) for collocation points $\boldsymbol{\xi}$ on either side of the crack, say $\partial\Omega_c^+$ (i.e., $\boldsymbol{\xi} \in \partial\Omega_c^+$):

$$p_j(\boldsymbol{\xi}) + \oint\!\!\!\!\!\!-_{\partial\Omega_e} s_{ij}^*(\mathbf{x},\boldsymbol{\xi})u_j(\mathbf{x})dS(\mathbf{x}) + \oint\!\!\!\!\!\!-_{\partial\Omega_c^+} s_{ij}^*(\mathbf{x},\boldsymbol{\xi})\Delta u_j(\mathbf{x})dS(\mathbf{x}) = \int_{\partial\Omega_e} d_{ij}^*(\mathbf{x},\boldsymbol{\xi})p_j(\mathbf{x})dS(\mathbf{x}) \tag{38}$$

Eqs. (37) and (38) yield a complete set of equations to compute the displacements and tractions on $\partial\Omega_e$ and the crack opening displacements $\Delta u_i = u_i^+ - u_i^-$ on $\partial\Omega_c$. In Eq. (38) the free term has been set to 1 because of the additional singularity arising from the coincidence of the two crack surfaces.

Numerical evaluation of the TBIE requires C^1 continuity of the displacements. As in previous works [27], discontinuous quadratic elements with the two extreme collocation nodes shifted towards the element interior are used to mesh the cracks. The asymptotic behavior of the displacements near the crack tip are modeled via discontinuous quarter-point elements. For the rest of the boundaries, continuous quadratic elements are employed. A detailed justification of the discretization procedure together with the integration scheme implemented and the expressions of the fundamental solutions, may be found in García-Sáchez et al. [27].

A collocation procedure on boundary integral equations (37) and (38) leads to the following system of equations: $\bar{\mathbf{A}}\mathbf{x} = \bar{\mathbf{F}}$, where the boundary conditions have been imposed and all the unknowns have been passed to vector $\mathbf{x}$, to yield

$$\begin{bmatrix} \bar{\mathbf{A}}_{\mathbf{x}_e} & \bar{\mathbf{A}}_{\Delta u_c} \end{bmatrix} \begin{Bmatrix} \mathbf{x}_e \\ \Delta\mathbf{u}_c \end{Bmatrix} = \bar{\mathbf{F}}. \tag{39}$$

In expression (39), $\mathbf{x}_e$ collects the nodal external unknowns (i.e. the nodal unknowns on $\partial\Omega_e$) and $\Delta\mathbf{u}_c$ collects the nodal crack opening displacements. Moreover, due to the fact that in all the numerical examples analyzed herein the MWCNT/epoxy composite plate is subjected to crack opening loads, no crack-face contact conditions have been considered in Eq. (39). At any event, without loss of generality, the resolution of a general cracked domain involving crack-face contact conditions could be easily implemented in the present scheme [50].

Finally, Mode-I and Mode-II stress intensity factors (K_I, K_{II}) (SIF) are directly computed from the nodal values of the crack opening displacements across the crack, at the closest collocation node to the crack-tip by following the approach proposed by the authors in [27].

$$\left(\begin{array}{c} K_{II} \\ K_I \end{array} \right) = 2\sqrt{2\pi/L}\,\mathbf{Y}^{-1} \left(\begin{array}{c} \Delta u_1 \\ \Delta u_2 \end{array} \right), \tag{40}$$

where $\mathbf{Y}$ is the compliance (Irwin) matrix defined in [27] and L is the length of the crack tip extreme quarter-point element.

3.3. Resistivity changes detection scheme

The dual BE formulation summarized above permits to numerically solve any fracture mechanics problem in CNT-reinforced composites. So, once the displacements and tractions are known on the boundary ($\partial\Omega$), the strain field in the domain of the plate Ω can be computed as: $\varepsilon_{ij} = (u_{i,j} + u_{j,i})/2$, being:

$$u_{i,m}(\boldsymbol{\xi}) = \int_{\partial\Omega} u^*_{ij,m}(\mathbf{x},\boldsymbol{\xi}) p_j(\mathbf{x}) dS(\mathbf{x}) - \int_{\partial\Omega} p^*_{ij,m}(\mathbf{x},\boldsymbol{\xi}) u_j(\mathbf{x}) dS(\mathbf{x}). \tag{41}$$

In the expression above, the space derivatives have been taken with respect to the coordinates of the collocation point and have been applied to the fundamental solution tensors: u^*_{ij} and p^*_{ij}. Eq. (41) follows straightforwardly from the particularization of the DBIE (24) for internal points in the domain Ω.

Once the strain field is known in the cracked domain, the relative resistivity changes ($\mathbf{r} = \Delta\boldsymbol{\rho}/\rho_o$) can be computed according to the procedure formerly outlined in Section 2.3. Note that the micromechanics approach previously presented in Section 2.1. is used to predict the constitutive properties of MWCNT/epoxy composites. At the material level, percolation paths must be defined in a 3D space since it is hypothesized that no special aligning techniques are applied. Nevertheless, the subsequent structural analyses are bi-dimensional in nature, thereby Eq. (21) can be simplified to:

$$\left[\begin{array}{c} \Delta\rho_1/\rho_o \\ \Delta\rho_2/\rho_o \\ \Delta\rho_6/\rho_o \end{array} \right] = \left[\begin{array}{ccc} \lambda_{11} & \lambda_{12} & 0 \\ \lambda_{12} & \lambda_{22} & 0 \\ 0 & 0 & \lambda_{44} \end{array} \right] \left[\begin{array}{c} \varepsilon_{11} \\ \varepsilon_{22} \\ 2\varepsilon_{12} \end{array} \right]. \tag{42}$$

3.4. Electric potential distribution and electric resistance changes

Once the strains have been computed inside the domain and, therefore, the non-homogeneous electrical conductivity (or its inverse, the electrical resistivity) is known at each internal point, it is possible to solve the corresponding electric problem to characterize how the presence of the crack does affect the piezoresistive performance of the CNT-reinforced composite sensor.

To this end, the electrostatic field in a non-homogenous domain can be computed, in absence of space-charge density, solving the partial differential equation,

$$\nabla \cdot (\boldsymbol{\kappa} \nabla \phi) = 0, \tag{43}$$

that describes the potential (ϕ) distribution within a given region Ω_{el} characterized by a non-homogenous electric conductivity tensor $\boldsymbol{\kappa}$, which can be computed as $\boldsymbol{\kappa} = \boldsymbol{\rho}^{-1}$. Due to the piezoelectric behavior of the CNT-reinforced composite material, its non-homogenous electric resistivity tensor can be computed as discussed above [15, 30], form:

$$\boldsymbol{\rho} = \rho_o(\mathbf{I} + \mathbf{r}) = \rho_o(\mathbf{I} + \boldsymbol{\Pi}\boldsymbol{\varepsilon}). \tag{44}$$

Adopting the electrodes configuration presented in Fig.4, one simple way to quantify the electric resistivity changes induced by the presence of a crack in the strip-like sensor would be to evaluate the electric resistance between

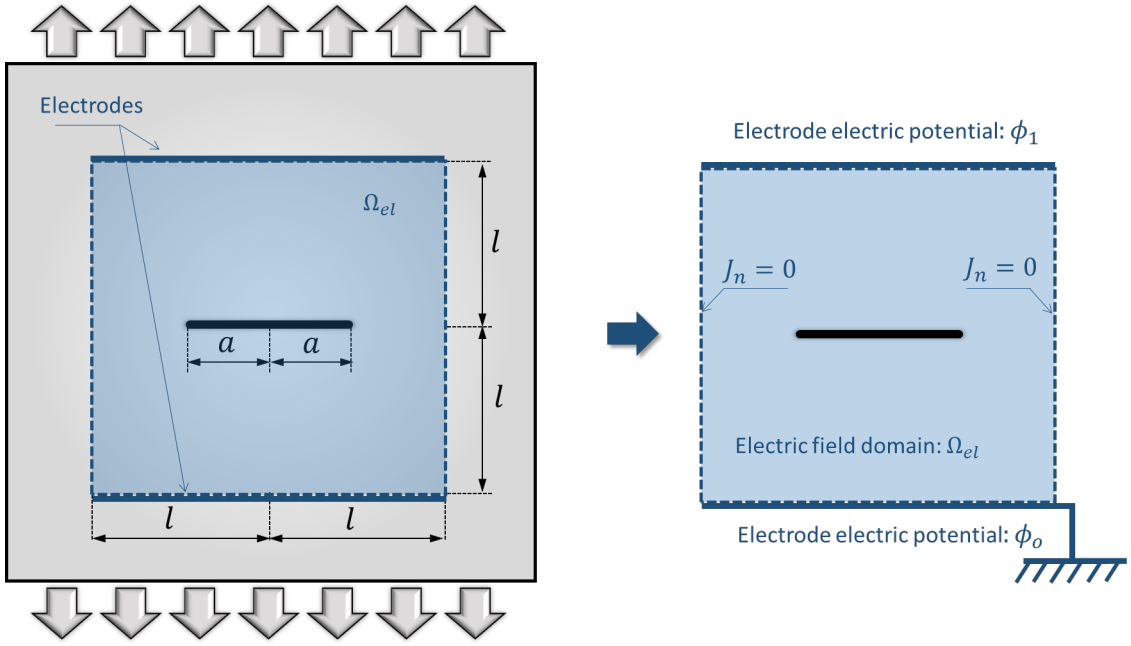

Figure 4: Electrodes position and electric field domain considered to study the crack-induced resistivity changes in cracked MWCNT/epoxy composite plate under uniform stress.

electrodes (R) of the damaged plate and compare its value with the electric resistance measured for the undamaged plate (R_o). The electric resistance (R) of a plate of thickness t can be computed as

$$R = \frac{\Delta\phi}{I}, \tag{45}$$

where $\Delta\phi = \phi_1 - \phi_o$ is the voltage difference recorded from electrodes and I is the electric current flowing through the sensor, which may be computed from the electric flux density $\mathbf{J}$ ($\mathbf{J} = -\boldsymbol{\kappa}\nabla\phi$)as

$$I = \int_A \mathbf{J}\mathbf{n} dA \approx \int_{-l}^{+l} \mathbf{J}\mathbf{n} t dx. \tag{46}$$

It should be emphasized that, even though the mechanical problem (22-41) is homogeneous, due to the piezoresitive behavior of the MWCNT reinforced composite (i.e. elastic deformations cause electrical conductivities variations) and to the electrical-conductivity discontinuities produced by the crack, the electrical problem (43-46) has to be solved under non-homogeneous electrical conductivities conditions.

In this paper, the resolution of the Eq. (43) is tackled, due to the non-homogenous electric conductivity properties, via the finite difference (FDM) scheme described in Appendix A. As previously explained, the values of the electric resistivity at each grid point of the FDM mesh are calculated from the strain values numerically computed using the dual BEM approach summarized above. Furthermore, the FDM mesh includes grid points coinciding with the location of the crack, where the crack-face electric permittivity conditions are directly imposed. in this manner, the influence of crack permittivity conditions ranging from impermeable crack conditions (vacuum inside the crack) to perfectly permeable crack conditions (presence of a conductive medium in the crack) can be easily analyzed in the results sections.

4. Numerical results

Several parametric studies are next conducted to illustrate the influence of various crack geometries in the piezoresistive behavior of a MWCNT/epoxy strip-like sensors. In particular, we analyze how it is affected by the presence of

Table 1: Effective electromechanical properties of smart MWCNT/epoxy strip-like sensor [14, 15].

wt%	$E(GPa)$	ν	$\kappa(S\,m^{-1})$	λ_{11}	λ_{12}	λ_{44}
0.5	2.86	0.28	1.22×10^{-2}	6.84	7.99	1.19
0.7	3.01	0.27	3.01×10^{-2}	4.85	6.01	1.19
1.0	3.23	0.27	6.56×10^{-2}	3.23	4.38	1.19

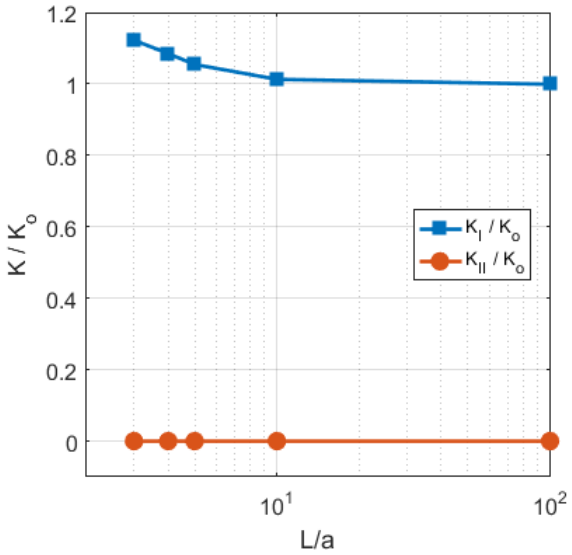

Figure 5: Influence of the crack size parameter (L/a) on the stress intensity factors: K_I/K_o and K_{II}/K_o, being $K_o = \bar{\sigma}_{yy}\sqrt{\pi a}$.

a crack at varying CNTs concentrations and crack electric permeability conditions. For this purpose, a MWCNT/epoxy composite square plate ($2L \times 2L$) under uniform stress ($\bar{\sigma}_{yy} = 1\ MPa$) is studied (see Fig.3). The plate presents a finite straight crack along the x-direction whose length is $2a$ ($a = 0.1\ m$). This problem is devised to characterize how the piezo-resistive behavior of the MWCNT/epoxy strip-like sensor [14, 15] is modified due to the presence of damage, and thus establish its validity range when cracked. In this example, we have considered a MWCNT/epoxy composite with filler contents moderately far from the percolation threshold ($f_c \approx 0.3$ wt%), namely $f_c = \{0.5, 0.7, 1.0\}$ wt%. In this manner, we ensure: (i) a linear strain sensitivity of the sensor, and (ii) the accuracy of the approach implemented to model the piezoresistive behavior of the composite [15, 30]. Based on [15], the values of the material constants are given in Table 1.

Moreover, several crack sizes are also considered, ranging from a crack in an infinite domain configuration ($L/a \geq 10$) to a severely cracked plate ($L/a = 3$). In Fig.5 we can observe the influence of the crack size parameter (L/a) on the stress intensity factors: K_I/K_o and K_{II}/K_o, being $K_o = \bar{\sigma}_{yy}\sqrt{\pi a}$. The stress and strain fields are illustrated in Fig.6: Fig.6 (a) shows the σ_{yy} stress distribution (relative to the prescribed stress $\bar{\sigma}_{yy}$) for $L/a = 10$ and $L/a = 3$, whereas Fig.6 (b) presents the ε_{yy} strain distribution relative to the undamaged uniform strain $\bar{\varepsilon}_{yy}$ for the cases: $L/a = 10$ and $L/a = 3$.

4.1. Resistivity changes: influence of the strain field

According to Eq.(42), the strain field computed in our cracked domain causes changes in electric resistivity. To quantify the severity of these changes, the relative resistivity change ($\Delta\rho_2/\rho_o$) is presented in Fig.7(a) and Fig.7(b) for $L/a = 10$ and $L/a = 3$, respectively. Both distributions look very similar. However, it is much more interesting to see how the piezoresistive behavior of the MWCNT/epoxy strip-like sensors is affected by the presence of a crack. For this purpose, Fig.8 shows the resistivity changes due to the crack ($\Delta\rho_2/\rho_o$), relative to those corresponding to the undamaged plate ($\Delta\rho_{2,o}/\rho_o$), under several L/a ratios. We can observe in Fig.9 that the resistivity variation at $x = 2.5a$

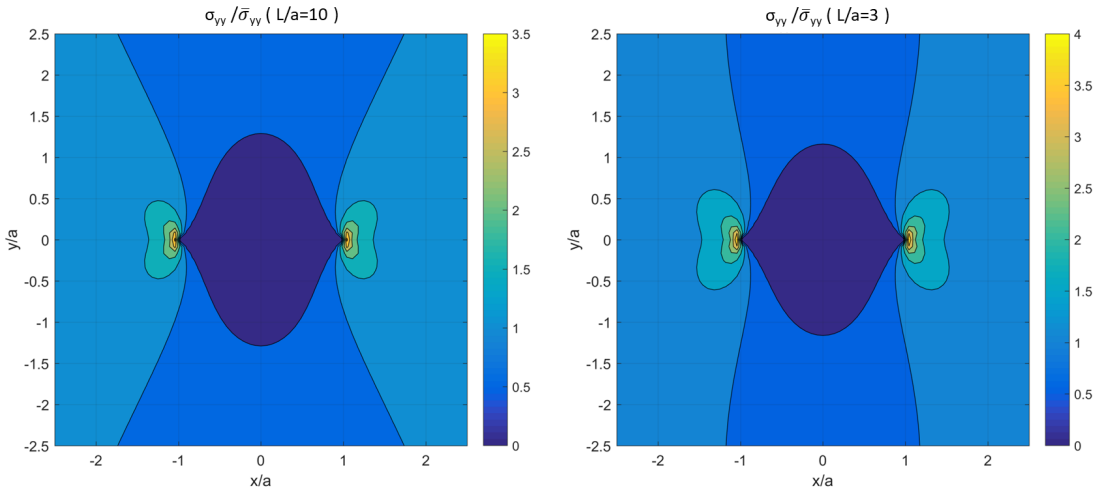

(a)

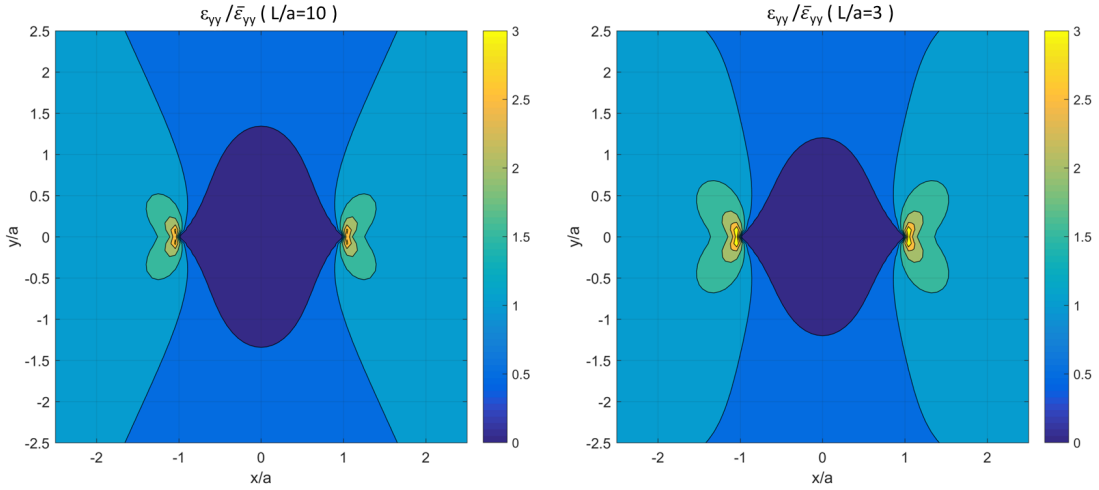

(b)

Figure 6: (a) σ_{yy} stress distribution for $L/a = 10$ and $L/a = 3$. (b) ε_{yy} strain distribution relative to the undamaged uniform strain $\bar{\varepsilon}_{yy}$, for $L/a = 10$ and $L/a = 3$.

can reach values up to $20-25\%$ at $-a \leq y \leq +a$. These results are obtained assuming electrically perfectly permeable boundary conditions at the crack faces).

4.2. Resistivity changes: influence of the electric permittivity crack conditions

The electric conductivity tensor $\boldsymbol{\kappa}$ can be obtained as $\boldsymbol{\kappa} = \boldsymbol{\rho}^{-1}$, being $\boldsymbol{\rho}$ the electric resistivity computed according to Eq.(45). Afterward, the electric potential distribution is obtained from Eq.(44) and the electric flux density ($\mathbf{J} = -\boldsymbol{\kappa}\nabla\phi$) allows us to compute electric current I according to Eq.(46). The FDM based resolution is detailed in Appendix A).

In this context, it is important to consider the crack-face electric permittivity conditions, i.e., permeable, impermeable or semipermeable crack conditions. The crack permittivity is designed as κ_{cv} and its values oscillate between $\kappa_{cv} \approx 0$ (i.e., impermeable crack conditions) and $\kappa_{cv} \approx \kappa_o$ (i.e., perfectly permeable crack conditions), being κ_o the electric conductivity of the undamaged and the unstrained plate.

For the damaged plate $L/a = 3$, Fig.10 shows the influence of several electric permittivity crack conditions on the electric potential distribution. Fig.10(a) presents the electric potential distribution for quasi-perfectly permeable crack conditions ($\kappa_{cv}/\kappa_o = 0.5$), whereas Fig.10(c) shows the electric potential distribution for quasi-perfectly impermeable

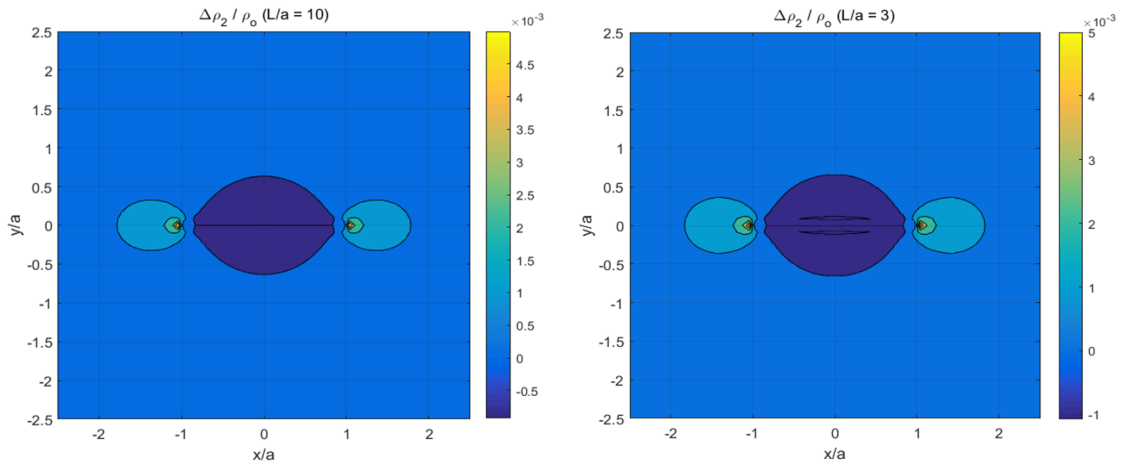

(a) (b)

Figure 7: Relative resistivity changes for the L/a ratios: (a) $L/a = 10$ and (b) $L/a = 3$.

crack conditions ($\kappa_{cv}/\kappa_o = 0.001$). We can observe that the electric field potential is clearly affected by the presence of a crack when impermeable or semipermeable crack conditions are considered. In other case, the electric potential distribution is almost the same as the distribution for the undamaged plate.

Same results can be observed in Fig.11, where the influence of the electrical permittivity conditions of the crack on the electric resistance R are presented for different CNT volume fractions for the experimental set-up sketched in Fig.4. Fig.11(a) shows the electric resistance (R) for different CNT volume fractions, relative to the electric resistance of the undamaged plate with 1.0 $wt\%$ ($R_{(o,1.0wt\%)}$). It can be observed an increment of the electric resistance when the CNT volume fraction is reduced. Fig.11(b) presents the electric resistance of the damaged plate (R) is divided by the electric resistance of the undamaged plate (R_o), according to their corresponding CNT volume fractions. A electric resistance increment is computed when impermeable or semipermeable crack conditions are considered. However, no electric resistance increment is observed (i.e., $R/R_o = 1$) when perfectly permeable crack conditions are assumed, in spite of the resistivity changes due to the strain field were considered. Moreover, the R/R_o value tends to a constant value ($R/R_o \approx 1.18$) when the permittivity values of the crack goes to zero (i.e., impermeable crack conditions). The same R/R_o behavior is observed for the different CNT volume fractions considered herein.

Finally, the distribution of the components of the non-homogenous electric conductivity tensor ($\boldsymbol{\kappa}$) under impermeable electric conductivity crack conditions on the damaged plate $L/a = 3$ can be observed in Fig.12.

4.3. Resistivity changes due to the crack size increment

To conclude this section, the influence of the crack size on the electric resistance changes in the damaged plate scheme presented in Fig.4 is studied. Fig.13 shows the influence of the the crack size parameter (l/a) on the electric resistance, taking into account the several electrical permittivity conditions on the crack. As we observed in Section 4.2, electric resistance increments are computed when impermeable or semipermeable crack conditions are considered. In all these cases (i.e., $\kappa_{cv}/\kappa_o < 1$), the resistance (R) increases with crack size (a), or in other words, with the decrease of the ratio l/a (see Fig.13).

The resulting electric potential distributions for two crack size values are presented in Fig.14. Fig.14(a) shows the electric potential distributions due to the presence of an impermeable crack with $l/a = 2.50$ and Fig.14(b) presents the electric potential distribution caused by an impermeable crack with $l/a = 1.25$. It is clear that the electric field is clearly affected by the crack size.

5. Summary and conclusions

This work presents a numerical framework to quantify the electrical resistivity changes in CNT-reinforced composites induced by the presence of cracks. Previous studies demonstrated the potential of MWCNT/epoxy strip-like

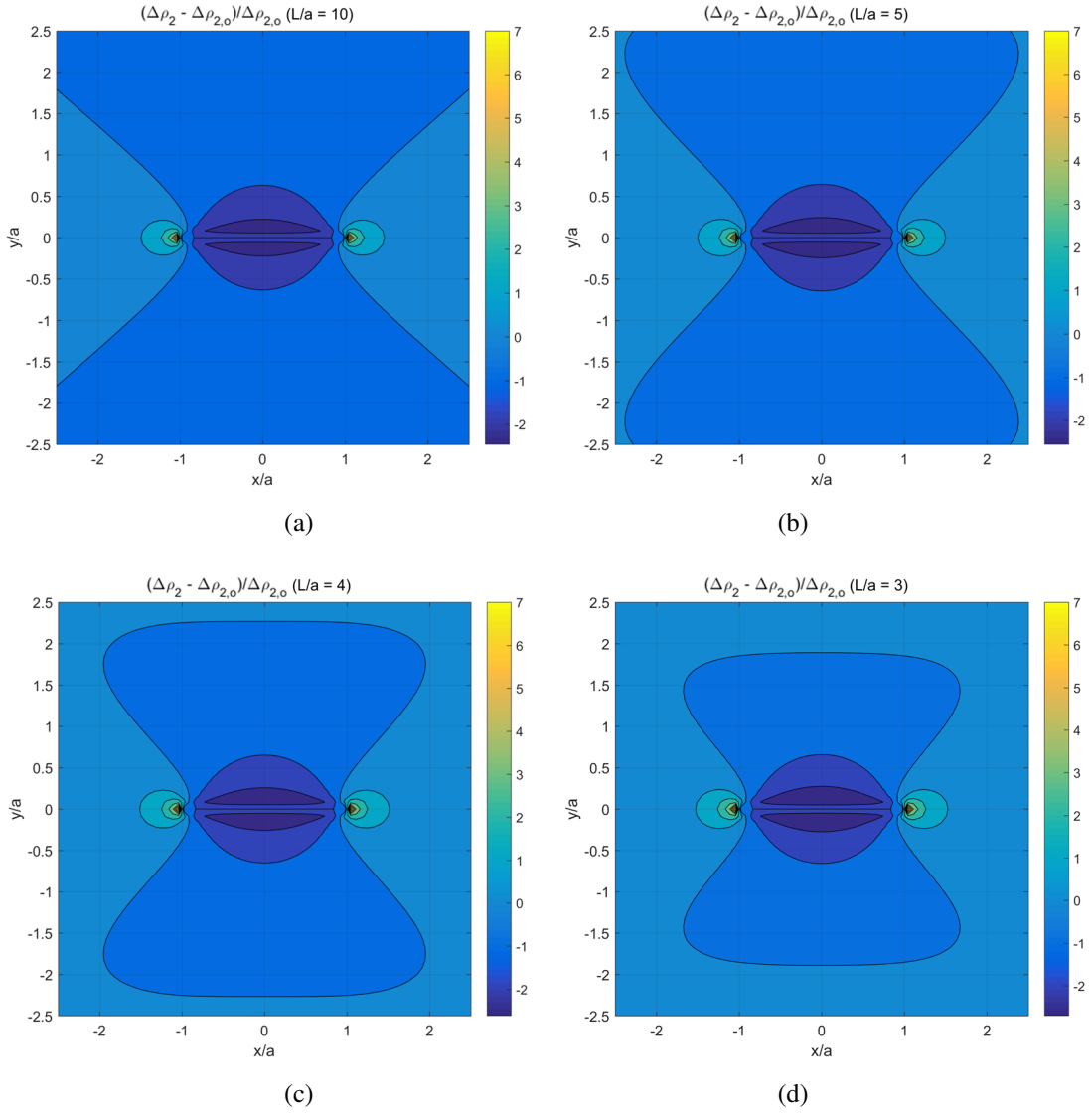

Figure 8: Resistivity changes due to the crack, relative to the undamaged plate, under several L/a ratios: (a) $L/a = 10$, (b) $L/a = 5$, (c) $L/a = 4$, (d) $L/a = 3$.

piezoresistive sensors for monitoring and damage detection in structures [14, 15]. Here, we aim at characterizing to which extent cracking in the sensor alters its performance. In this way, a dual BE approach has been proposed in order to accurately compute the strain in the cracked domain and, subsequently -by substituting the strains in Eq. (42)- determine the electrical resistivity at each point of such cracked domain [30]. Finally, a finite difference scheme has been implemented to solve the electric field and compute the resulting electric resistance caused by the presence of a crack in the MWCNT/epoxy strip-like strain sensors.

Three parameters can affect the efficiency of the sensitive skin sensor due to electrical resistance changes:

- the strain field around the crack alters the electric resistivity due to the piezo-resistive behavior of the MWCNT/epoxy composite,
- the electric permeability of the crack is a key factor in the electric conductivity response
- and finally, the severity of the damage, i.e., the crack size.

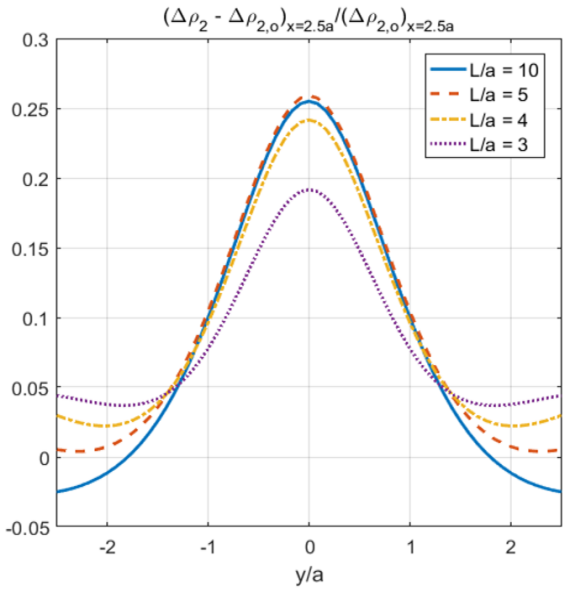

Figure 9: Resistivity changes relative to the undamaged plate under several L/a ratios at $x = 2.5a$.

Results reveal that the strain gradients caused by the crack affect the resistivity of the plate when they are compared to the crack without damage. However, they are not as significant as those that appear due to the discontinuity in the electrical conductance that the crack causes in the domain.

The influence of the electric permeability of the crack has revealed as a key parameter that controls the efficiency of the strip-like sensor, i.e., that determines the behavior of the electric resistance of the plate. Section 4.2 has showed the electric resistance increment (or the reduction of the electrical conductance) due to the presence of an impermeable or a semipermeable crack. Moreover, the severity of the damage also greatly affects the electric conductance of the sensing-plate. Section 4.3 has clearly illustrated the important changes in the electrical resistance of the sensor when the crack size increases.

Therefore, the obtained results show that the efficiency of the structural health monitoring scheme based on a MWCNT/epoxy sensing-skin [14, 15] is clearly affected by the presence of damage. A crack in the sensing plate increases the electrical resistance and therefore distorts the measurements. So prediction protocols have to be established to detect damage in these systems. The numerical scheme presented in this work makes it possible to quantify the electrical resistance changes in these sensors (due to the presence of a crack) and it can serve as a numerical tool to assist in establishing such prediction protocols.

Finally, the resistance changes computing scheme presented in this work could be extended for self-sensing structures developments (for instance, application in carbon fiber reinforced composite panels) or other structures of great interest in the civil or aeronautical industries.

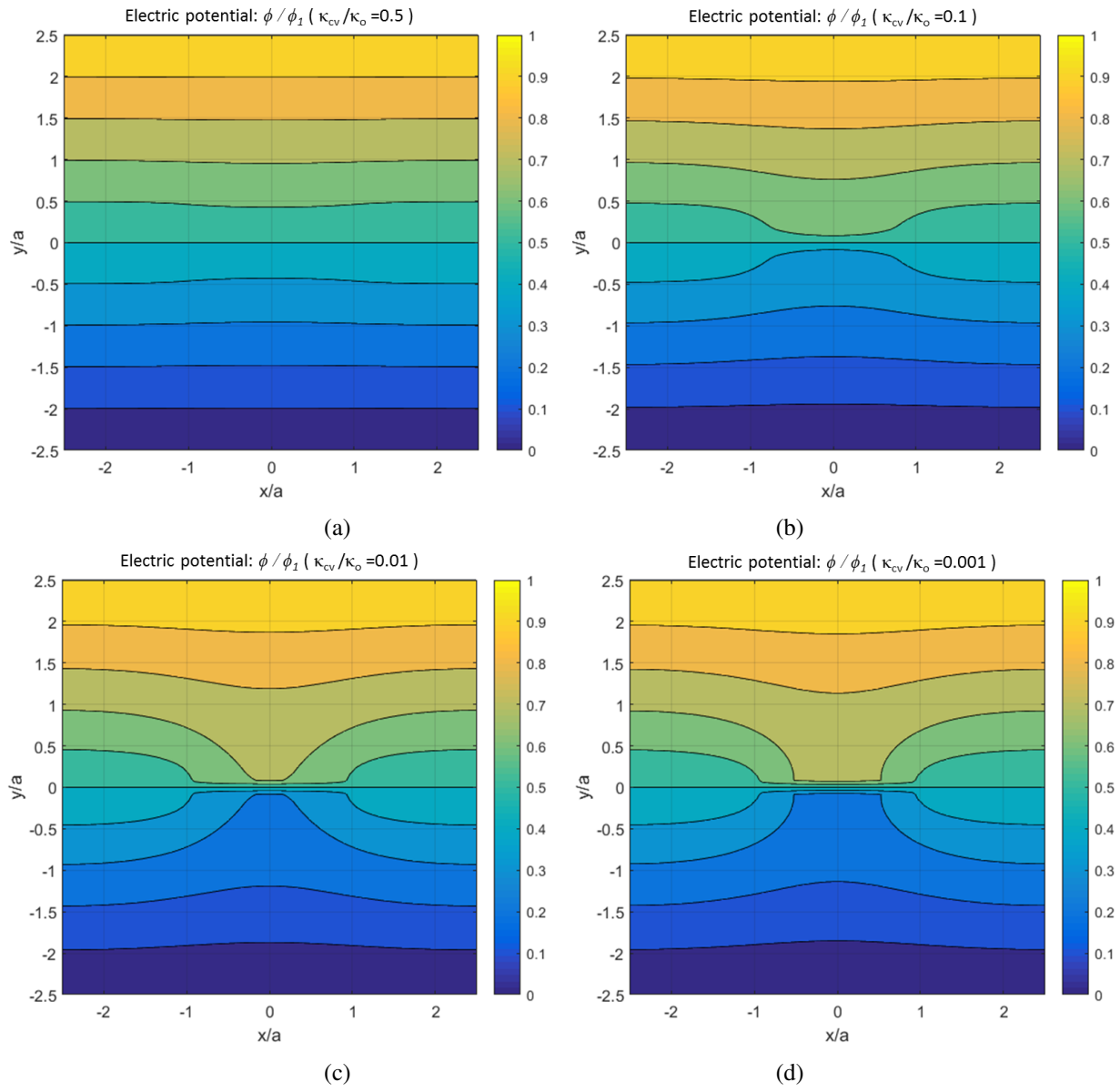

Figure 10: Electric potential distribution for several electric permittivity crack conditions: (a) $\kappa_{cv}/\kappa_o = 0.5$, (b) $\kappa_{cv}/\kappa_o = 0.1$, (c) $\kappa_{cv}/\kappa_o = 0.01$, (d) $\kappa_{cv}/\kappa_o = 0.001$.

6. Acknowledgments

This work was supported by the Ministerio de Economía y Competitividad of Spain and the European Regional Development Fund under projects RTI2018-094945-B-C21 and DPI2017-89162-R. The financial support is gratefully acknowledged.

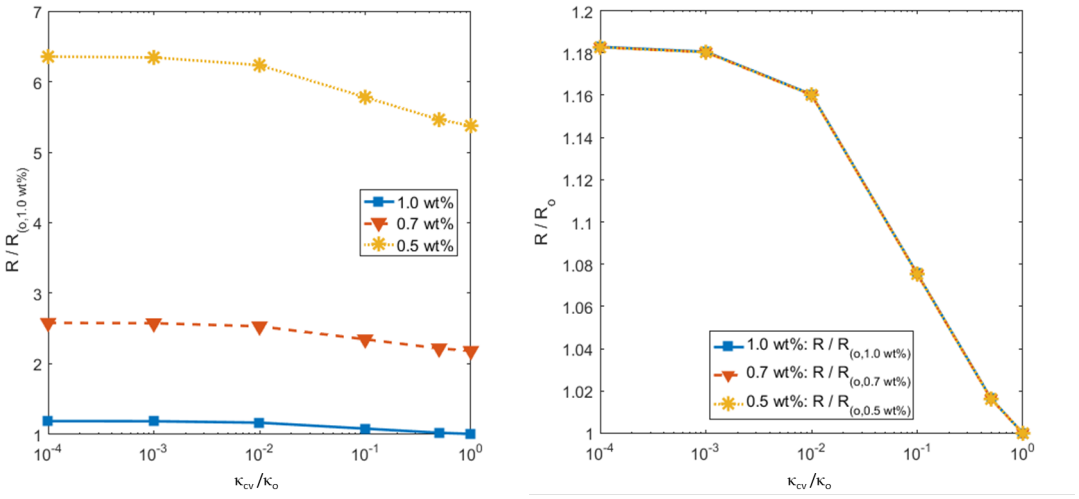

(a) (b)

Figure 11: Influence of the electrical permittivity conditions of the crack on the electric resistance (R) for different CNT volume fractions: (a) relative to the electric resistance of the undamaged plate with 1.0 $wt\%$ ($R_{(o,1.0wt\%)}$) and (b) relative to the undamaged resistance of its own CNT volume fractions.

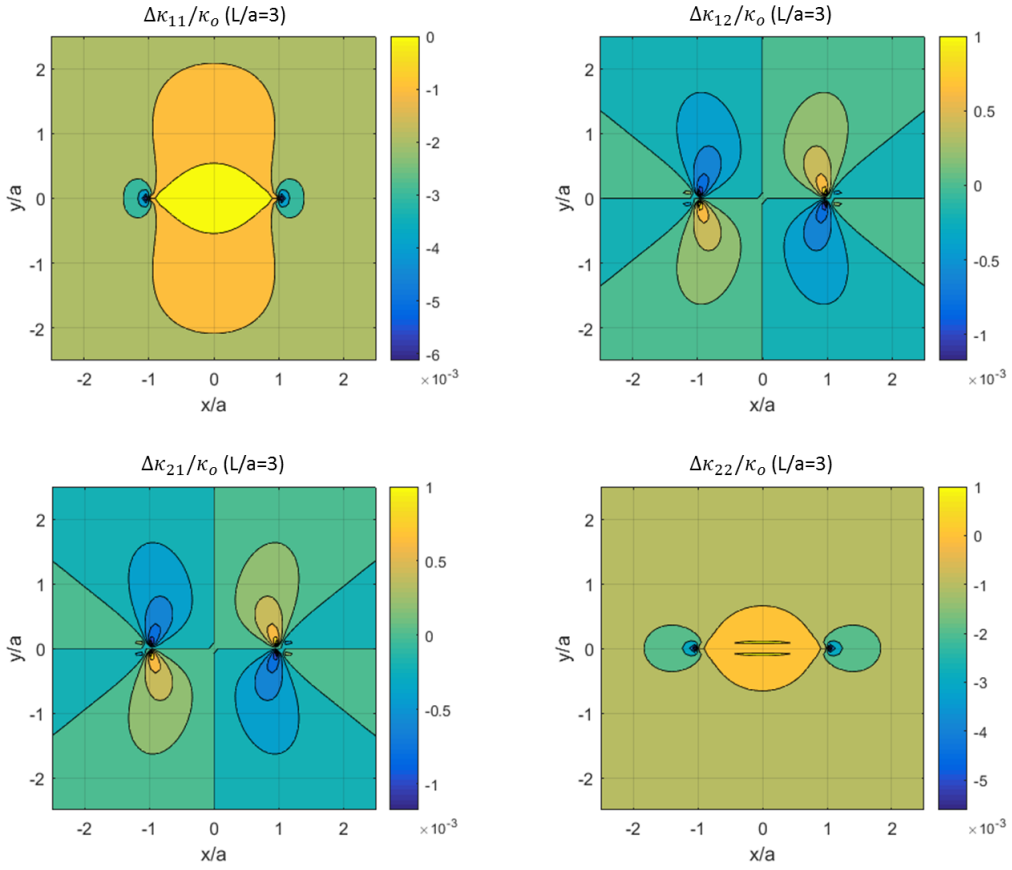

Figure 12: Distribution of the components of the non-homogenous electric conductivity tensor ($\boldsymbol{\kappa}$)under impermeable electric conductivity crack conditions on the damaged plate $L/a = 3$.

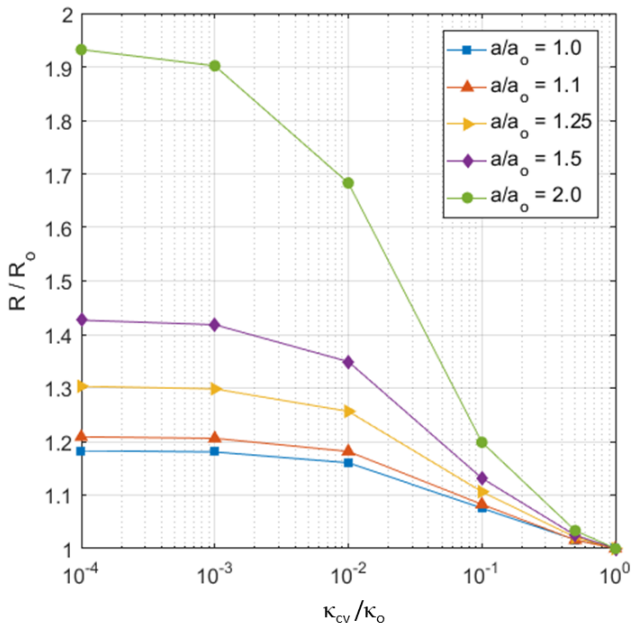

Figure 13: Influence of the the size of the crack on the electric resistance changes.

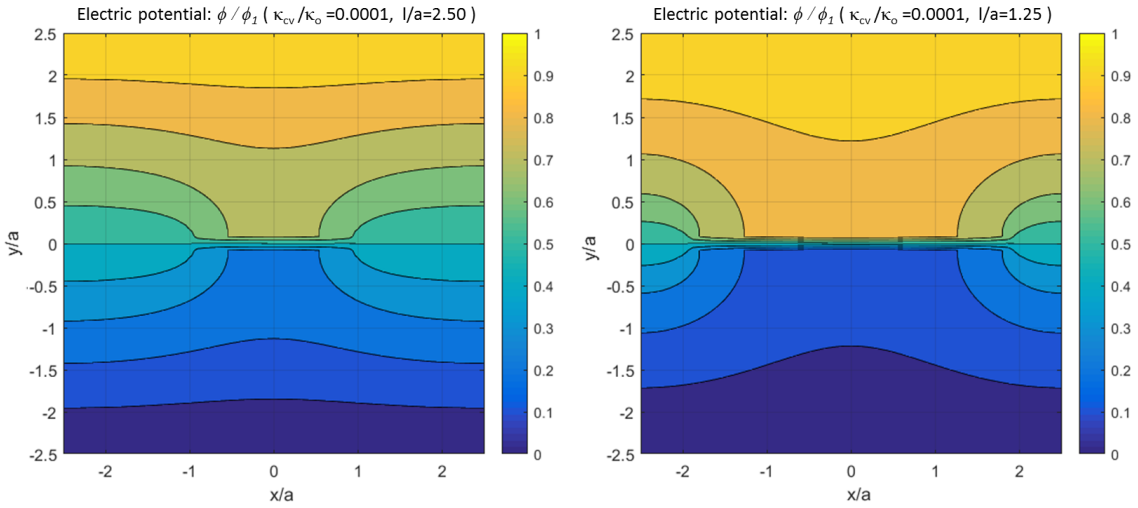

(a) (b)

Figure 14: Influence of the crack size a in the electric potential distributions due to the presence of a crack for the l/a ratios: (a) $l/a = 2.50$ and (b) $l/a = 1.25$.

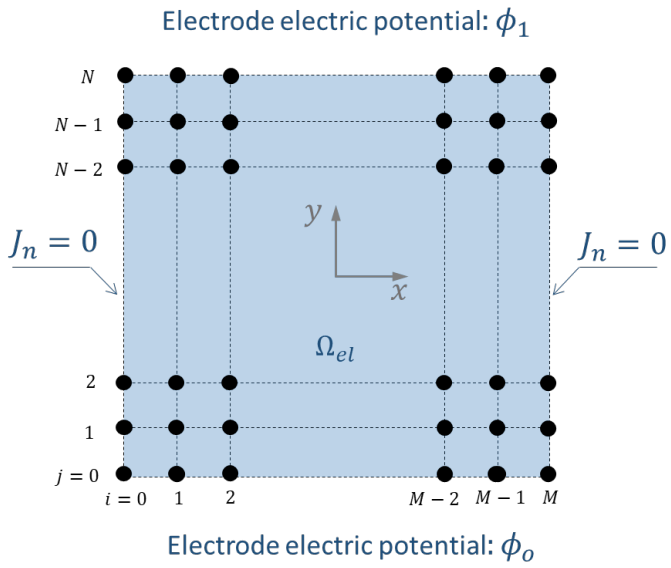

Figure 15: A schematic showing the FDM mesh numbering.

A. Finite difference method for non-homogenous conductivity distribution

The electrostatic field in a non-homogenous conductivity distribution domain can be computed, in absence of space-charge density, solving Eq.(43). This equation can be written as

$$\begin{bmatrix} \partial/\partial x & \partial/\partial y \end{bmatrix} \left(\begin{bmatrix} \kappa_{11} & \kappa_{12} \\ \kappa_{21} & \kappa_{22} \end{bmatrix} \begin{bmatrix} \partial\phi/\partial x \\ \partial\phi/\partial y \end{bmatrix} \right) = 0. \tag{47}$$

Derivatives in the partial differential equation Eq.(47) are approximated by linear combinations of function values at the grid points (see Fig.15) as

$$\frac{\partial}{\partial x}\left(\kappa_{11}\frac{\partial\phi}{\partial x}\right) \approx \frac{1}{2\Delta x}\left(\kappa_{11}|_{i+\frac{1}{2},j}\frac{\phi_{i+1,j}-\phi_{i,j}}{\Delta x} + \kappa_{11}|_{i-\frac{1}{2},j}\frac{\phi_{i-1,j}-\phi_{i,j}}{\Delta x}\right), \tag{48}$$

$$\frac{\partial}{\partial x}\left(\kappa_{12}\frac{\partial\phi}{\partial y}\right) \approx \frac{1}{2\Delta x}\left(\kappa_{12}|_{i+\frac{1}{2},j}\frac{\phi_{i,j+1}-\phi_{i,j}}{\Delta y} + \kappa_{12}|_{i-\frac{1}{2},j}\frac{\phi_{i,j-1}-\phi_{i,j}}{\Delta y}\right), \tag{49}$$

$$\frac{\partial}{\partial y}\left(\kappa_{21}\frac{\partial\phi}{\partial x}\right) \approx \frac{1}{2\Delta y}\left(\kappa_{21}|_{i,j+\frac{1}{2}}\frac{\phi_{i+1,j}-\phi_{i,j}}{\Delta x} + \kappa_{21}|_{i,j-\frac{1}{2}}\frac{\phi_{i-1,j}-\phi_{i,j}}{\Delta x}\right), \tag{50}$$

$$\frac{\partial}{\partial y}\left(\kappa_{22}\frac{\partial\phi}{\partial y}\right) \approx \frac{1}{2\Delta y}\left(\kappa_{22}|_{i,j+\frac{1}{2}}\frac{\phi_{i,j+1}-\phi_{i,j}}{\Delta y} + \kappa_{22}|_{i,j-\frac{1}{2}}\frac{\phi_{i,j-1}-\phi_{i,j}}{\Delta y}\right), \tag{51}$$

where constant values are assumed for Δx and Δy (i.e., $x_{i+1} = x_i + \Delta x$ and $y_{j+1} = y_j + \Delta y$, and

$$\kappa_{11}|_{i+\frac{1}{2},j} = (\kappa_{11}|_{i+1,j} + \kappa_{11}|_{i,j})/2, \quad \kappa_{11}|_{i-\frac{1}{2},j} = (\kappa_{11}|_{i-1,j} + \kappa_{11}|_{i,j})/2 \tag{52}$$

$$\kappa_{12}|_{i+\frac{1}{2},j} = (\kappa_{12}|_{i+1,j} + \kappa_{12}|_{i,j})/2, \quad \kappa_{12}|_{i-\frac{1}{2},j} = (\kappa_{12}|_{i-1,j} + \kappa_{12}|_{i,j})/2 \tag{53}$$

$$\kappa_{21}|_{i,j+\frac{1}{2}} = (\kappa_{21}|_{i,j+1} + \kappa_{21}|_{i,j})/2, \quad \kappa_{21}|_{i,j-\frac{1}{2}} = (\kappa_{21}|_{i,j-1} + \kappa_{21}|_{i,j})/2 \tag{54}$$

$$\kappa_{22}|_{i,j+\frac{1}{2}} = (\kappa_{22}|_{i,j+1} + \kappa_{22}|_{i,j})/2, \quad \kappa_{22}|_{i,j-\frac{1}{2}} = (\kappa_{22}|_{i,j-1} + \kappa_{22}|_{i,j})/2 \tag{55}$$

Substituting the linear combination of the function values at the grid points (48-40) into Eq.(47) allows us to obtain the finite difference equation of Eq.(47):

$$b_-\phi_{i,j-1} + a_-\phi_{i-1,j} - \bar{a}\phi_{i,j} + a_+\phi_{i+1,j} + b_+\phi_{i,j+1}, \tag{56}$$

being $\bar{a} = a_+ + a_- + b_+ + b_-$ and

$$a_+ = \frac{\kappa_{11}|_{i+\frac{1}{2},j}}{2\Delta x^2} + \frac{\kappa_{21}|_{i,j+\frac{1}{2}}}{2\Delta x \Delta y}, \quad a_- = \frac{\kappa_{11}|_{i-\frac{1}{2},j}}{2\Delta x^2} + \frac{\kappa_{21}|_{i,j-\frac{1}{2}}}{2\Delta x \Delta y}, \tag{57}$$

$$b_+ = \frac{\kappa_{12}|_{i+\frac{1}{2},j}}{2\Delta x \Delta y} + \frac{\kappa_{22}|_{i,j+\frac{1}{2}}}{2\Delta y^2}, \quad b_- = \frac{\kappa_{12}|_{i-\frac{1}{2},j}}{2\Delta x \Delta y} + \frac{\kappa_{22}|_{i,j-\frac{1}{2}}}{2\Delta y^2}, \tag{58}$$

The boundary conditions are described in Fig.15, so Eq.(56) can be written as

$$\begin{bmatrix} \mathbf{A} & \mathbf{B}_+ & \mathbf{0} & \cdots & \mathbf{0} \\ \mathbf{B}_- & \mathbf{A} & \mathbf{B}_+ & \ddots & \vdots \\ \mathbf{0} & \ddots & \ddots & \ddots & \mathbf{0} \\ \vdots & \ddots & \mathbf{B}_- & \mathbf{A} & \mathbf{B}_+ \\ \mathbf{0} & \cdots & \mathbf{0} & \mathbf{B}_- & \mathbf{A} \end{bmatrix} \begin{Bmatrix} \boldsymbol{\phi}_1 \\ \boldsymbol{\phi}_2 \\ \vdots \\ \boldsymbol{\phi}_{N-2} \\ \boldsymbol{\phi}_{N-1} \end{Bmatrix} = \begin{Bmatrix} -\mathbf{B}_- \bar{\boldsymbol{\phi}}_0 \\ \mathbf{0} \\ \vdots \\ \mathbf{0} \\ -\mathbf{B}_+ \bar{\boldsymbol{\phi}}_N \end{Bmatrix} \tag{59}$$

where

$$\mathbf{A} = \begin{bmatrix} -\bar{a} & a_+ + a_- & 0 & \cdots & 0 \\ a_- & -\bar{a} & a_+ & \ddots & \vdots \\ 0 & \ddots & \ddots & \ddots & 0 \\ \vdots & \ddots & a_- & -\bar{a} & a_+ \\ 0 & \cdots & 0 & a_+ + a_- & -\bar{a} \end{bmatrix}, \; \mathbf{B}_+ = \begin{bmatrix} b_+ & 0 & \cdots \\ 0 & \ddots & 0 \\ \vdots & 0 & b_+ \end{bmatrix}, \; \mathbf{B}_- = \begin{bmatrix} b_- & 0 & \cdots \\ 0 & \ddots & 0 \\ \vdots & 0 & b_- \end{bmatrix}, \tag{60}$$

$$\boldsymbol{\phi}_j = \begin{Bmatrix} \phi_{0,j} \\ \vdots \\ \phi_{i,j} \\ \vdots \\ \phi_{M,j} \end{Bmatrix}, \; \bar{\boldsymbol{\phi}}_0 = \begin{Bmatrix} \phi_0 \\ \vdots \\ \phi_0 \\ \vdots \\ \phi_0 \end{Bmatrix}, \; \bar{\boldsymbol{\phi}}_M = \begin{Bmatrix} \phi_1 \\ \vdots \\ \phi_1 \\ \vdots \\ \phi_1 \end{Bmatrix}, \tag{61}$$

and ϕ_0 and ϕ_1 are the prescribed electric potentials showed in Fig.15.

The system of equations (59) allow us to obtain the electric potential (ϕ) on every grid point. So the electric current (I) in our plate of thickness t can be obtained as,

$$I = \int_{-l}^{+l} \mathbf{J}\mathbf{n} t dx = \int_{-l}^{+l} J_y \, t \, dx \approx \sum_{i=1}^{M} (J_y)_{i,j} \, t \, dx. \tag{62}$$

where the y-component of the electric flux density is computed as

$$(J_y)_{i,j} = \kappa_{21}|_{i,j} \frac{\phi_{i+1,j} - \phi_{i-1,j}}{2\Delta x} + \kappa_{22}|_{i,j} \frac{\phi_{i,j+1} - \phi_{i,j-1}}{2\Delta y}. \tag{63}$$

Finally, the resistance (R) of our plate is obtained as,

$$R = \frac{\phi_1 - \phi_o}{I}. \tag{64}$$

References

[1] Erik T Thostenson and Tsu-Wei Chou. Real-time in situ sensing of damage evolution in advanced fiber composites using carbon nanotube networks. *Nanotechnology*, 19(21):215713, apr 2008.

[2] Xun Yu and Eil Kwon. A carbon nanotube/cement composite with piezoresistive properties. *Smart Materials and Structures*, 18(5):055010, mar 2009.
[3] Haibo Zhao, Yingying Zhang, Philip D Bradford, Qian Zhou, Quanxi Jia, Fuh-Gwo Yuan, and Yuntian Zhu. Carbon nanotube yarn strain sensors. *Nanotechnology*, 21(30):305502, jul 2010.
[4] Alamusi, Ning Hu, Hisao Fukunaga, Satoshi Atobe, Yaolu Liu, and Jinhua Li. Piezoresistive strain sensors made from carbon nanotubes based polymer nanocomposites. *Sensors*, 11(11):10691–10723, 2011.
[5] J.K.W. Sandler, J.E. Kirk, I.A. Kinloch, M.S.P. Shaffer, and A.H. Windle. Ultra-low electrical percolation threshold in carbon-nanotube-epoxy composites. *Polymer*, 44:5893–5899, 2003.
[6] A. Sanli, A. Benchirouf, C. Mller, and O. Kanoun. Piezoresistive performance characterization of strain sensitive multi-walled carbon nanotube-epoxy nanocomposites. *Sensors and Actuators, A: Physical*, 254:61–68, 2017.
[7] J. Sebastian, N. Schehl, M. Bouchard, M. Boehle, L. Li, A. Lagounov, and K. Lafdi. Health monitoring of structural composites with embedded carbon nanotube coated glass fiber sensors. *Carbon*, 66:191 – 200, 2014.
[8] Hongbo Dai, Erik T. Thostenson, and Thomas Schumacher. Processing and characterization of a novel distributed strain sensor using carbon nanotube-based nonwoven composites. *Sensors*, 15(7):17728–17747, 2015.
[9] Kai Ke, Vahab Solouki Bonab, Dian Yuan, and Ica Manas-Zloczower. Piezoresistive thermoplastic polyurethane nanocomposites with carbon nanostructures. *Carbon*, 139:52 – 58, 2018.
[10] I. Kang, M.J. Schulz, J.H. Kim, V. Shanov, and D. Shi. A carbon nanotube strain sensor for structural health monitoring. *Smart Materials and Structures*, 15:737–748, 2006.
[11] S. Luo, W. Obitayo, and T. Liu. SWCNT-thin-film-enabled fiber sensors for lifelong structural health monitoring of polymeric composites - From manufacturing to utilization to failure. *Carbon*, 76:321–329, 2014.
[12] L. Vertuccio, L. Guadagno, G. Spinelli, P. Lamberti, and V. Tucci S. Russo. Piezoresistive properties of resin reinforced with carbon nanotubes for health-monitoring of aircraft primary structures. *Composites Part B: Engineering*, 107:192–202, 2016.
[13] P.A. Carraro, M. Zappalorto, and M. Quaresimin. Health monitoring of cross-ply laminates: Modelling the correlation between damage evolution and electrical resistance change. *Composites Part A: Applied Science and Manufacturing*, 86:151–158, 2016.
[14] Enrique García-Macías, Luis Rodríguez, and Andrés Sáez. MWCNT/epoxy strip-like sensors for buckling detection in beam-like structures. *Thin-Walled Structures*, 133:27 – 41, 2018.
[15] Enrique García-Macías, Luis Rodríguez-Tembleque, Andrés Sáez, and Filippo Ubertini. Crack detection and localization in RC beams through smart MWCNT/epoxy strip-like strain sensors. *Smart Materials and Structures*, 27(11):115022, oct 2018.
[16] F.H. Gojny, M.H.G. Wichmann, U. Köpke, B. Fiedler, and K. Schulte. Carbon nanotube-reinforced epoxy-composites: Enhanced stiffness and fracture toughness at low nanotube content. *Composites Science and Technology*, 64:2363–2371, 2004.
[17] G. Ragosta, M. Abbate, P. Musto, G. Scarinzi, and L. Mascia. Epoxy-silica particulate nanocomposites: Chemical interactions, reinforcement and fracture toughness. *Polymer*, 46:10506–10516, 2005.
[18] L. Sun, R.F. Gibson, F. Gordaninejad, and J. Suhr. Energy absorption capability of nanocomposites: A review. *Composites Science and Technology*, 69:2392–2409, 2009.
[19] M.R. Ayatollahi, S. Shadlou, and M.M. Shokrieh. Fracture toughness of epoxy/multi-walled carbon nanotube nano-composites under bending and shear loading conditions. *Materials and Design*, 32:2115–2124, 2011.
[20] T.H. Hsieh, A.J. Kinloch, A.C. Taylor, and I.A. Kinloch. The effect of carbon nanotubes on the fracture toughness and fatigue performance of a thermosetting epoxy polymer. *Journal of Materials Science*, 46:7525–7535, 2011.
[21] L. C. Tang, H. Zhang, J. H. Han, X. P. Wu, and Z. Zhang. Fracture mechanisms of epoxy filled with ozone functionalized multi-wall carbon nanotubes. *Composites Science and Technology*, 72:7–13, 2011.
[22] N. Lachman, H. Qian, M. Houllé, J. Amadou, M.S.P. Shaffer, and H.D. Wagner. Fracture behavior of carbon nanotube/carbon microfiber hybrid polymer composites. *Journal of Materials Science*, 48:5590–5595, 2013.
[23] U.A. Joshi, S.C. Sharma, and S.P. Harsha. Analysis of fracture in carbon nanotube based composites using extended finite element method. *Journal of Computational and Theoretical Nanoscience*, 9:872–878, 2012.
[24] A. Fereidoon, M. Rajabpour, and H. Hemmatian. Fracture analysis of epoxy/SWCNT nanocomposite based on global-local finite element model. *Composites Part B: Engineering*, 54:400–408, 2013.
[25] Y. Li, S. Wang, Q. Wang, and M. Xing. Enhancement of fracture properties of polymer composites reinforced by carbon nanotubes: A molecular dynamics study. *Carbon*, 129:504–509, 2018.
[26] A. Negi, G. Bhardwaj, J.S. Saini, K. Khanna, and R.K. Godara. Analysis of CNT reinforced polymer nanocomposite plate in the presence of discontinuities using XFEM. *Theoretical and Applied Fracture Mechanics*, 103:102292, 2019.
[27] F. García-Sánchez, Andrés Sáez, and J. Domínguez. Anisotropic and piezoelectric materials fracture analysis by BEM. *Computers & Structures*, 83(10):804 – 820, 2005. Boundary Element Methods.
[28] M.H. Aliabadi. Boundary element formulations in fracture mechanics. *Applied Mechanics Reviews*, 50(2):83–96, 1997.
[29] Y.J. Liu, S. Mukherjee, N. Nishimura, M. Schanz, W. Ye, A. Sutradhar, E. Pan, N.A. Dumont, A. Frangi, and A. Saez. Recent advances and emerging applications of the boundary element method. *Applied Mechanics Reviews*, 64:031001, 2011.
[30] Enrique García-Macías, Rafael Castro-Triguero, Andrés Sáez, and Filippo Ubertini. 3D mixed micromechanics-FEM modeling of piezoresistive carbon nanotube smart concrete. *Computer Methods in Applied Mechanics and Engineering*, 340:396 – 423, 2018.
[31] Wenxiang Xu, Fan Wu, Yang Jiao, and Mingjun Liu. A general micromechanical framework of effective moduli for the design of nonspherical nano-and micro-particle reinforced composites with interface properties. *Materials & Design*, 127:162–172, 2017.
[32] Enrique García-Macías, Rafael Castro-Triguero, and Filippo Ubertini. Two-step hierarchical micromechanics model of partially saturated porous composites doped with ellipsoidal particles with interface effects. *Composites Part B: Engineering*, 148:49–60, 2018.
[33] Muneo Hori and Sia Nemat-Nasser. Double-inclusion model and overall moduli of multi-phase composites. *Mechanics of Materials*, 14(3):189–206, 1993.
[34] Wenxiang Xu, Huaifa Ma, Shunying Ji, and Huisu Chen. Analytical effective elastic properties of particulate composites with soft interfaces around anisotropic particles. *Composites Science and Technology*, 129:10–18, 2016.

[35] Toshio Mura. *Micromechanics of defects in solids*, volume 3. Springer Science & Business Media, 1987.
[36] Fei Deng and Q. S. Zheng. An analytical model of effective electrical conductivity of carbon nanotube composites. *Applied Physics Letters*, 92(7):071902, 2008.
[37] Chuang Feng and Liying Jiang. Micromechanics modeling of the electrical conductivity of carbon nanotube (CNT)–polymer nanocomposites. *Composites Part A: Applied Science and Manufacturing*, 47:143–149, 2013.
[38] John G Simmons. Generalized formula for the electric tunnel effect between similar electrodes separated by a thin insulating film. *Journal of Applied Physics*, 34(6):1793–1803, 1963.
[39] Gary D Seidel and Dimitris C Lagoudas. A micromechanics model for the electrical conductivity of nanotube-polymer nanocomposites. *Journal of Composite Materials*, 43(9):917–941, 2009.
[40] KY Yan, QZ Xue, QB Zheng, and LZ Hao. The interface effect of the effective electrical conductivity of carbon nanotube composites. *Nanotechnology*, 18(25):255705, 2007.
[41] G. M. Odegard and T. S. Gates. Constitutive modeling of nanotube/polymer composites with various nanotube orientation. In *2002 SEM Annual Conference on Experimental and Applied Mechanincs*, 2002.
[42] Enrique García-Macías, Antonella D'Alessandro, Rafael Castro-Triguero, Domingo Pérez-Mira, and Filippo Ubertini. Micromechanics modeling of the electrical conductivity of carbon nanotube cement-matrix composites. *Composites Part B: Engineering*, 108:451–469, 2017.
[43] Minoru Taya. *Electronic composites: modeling, characterization, processing, and MEMS applications*. Cambridge University Press, 2005.
[44] A.A. Barlian, W.-T. Park, A.J. Rastegar J.R. Mallon, and B.L. Pruitt. Review: Semiconductor piezoresistance for microsystems. *Proceedings of the IEEE*, 97(3):513–552, 2009.
[45] C. Feng and L. Y. Jiang. Investigation of uniaxial stretching effects on the electrical conductivity of CNT-polymer nanocomposites. *Journal of Physics D: Applied Physics*, 47(40):405103, 2014.
[46] Takashi Komori and Kunio Makishima. Numbers of fiber-to-fiber contacts in general fiber assemblies. *Textile Research Journal*, 47(1):13–17, 1977.
[47] AP Sobha and Sunil K Narayanankutty. Improved strain sensing property of functionalised multiwalled carbon nanotube/polyaniline composites in TPU matrix. *Sensors and Actuators A: Physical*, 233:98–107, 2015.
[48] H.-K. Hong and J.-T. Chen. Derivation of integral equations of elasticity. *J. Engrg. Mech. ASCE*, 114:1028 –1044, 1988.
[49] P. Sollero and M.H. Aliabadi. Anisotropic analysis of cracks in composite laminates using the dual boundary element method. *Composite Structures*, 31:229–233, 1995.
[50] L. Rodríguez-Tembleque, F. García-Sánchez, and A. Sáez. Crack-face frictional contact modelling in cracked piezoelectric materials. *Computational Mechanics*, 2019.